JGR Planets

RESEARCH ARTICLE

Key Points:

- We run simulations of stagnant-lid mixed-heated convection and build temperature and heat flux scaling laws from them
- Stagnant lid stiffens (its mobility decreases) and thins with increasing rate of internal heating
- The critical rate of internal heating at which bottom heat flux turns negative increases with increasing viscosity ratio

Scaling Laws for Mixed-Heated Stagnant-Lid Convection and Application to Europa

Frédéric Deschamps[1] and **Kenny Vilella[2]**

[1]Institute of Earth Sciences, Academia Sinica, Taipei, Taiwan, [2]JSPS International Research Fellow, Hokkaido University, Sapporo, Japan

Abstract Because rocks and ices viscosities strongly depend on temperature, planetary mantles and ice shells are often thought to be animated by stagnant-lid convection. Their dynamics is further impacted by the release of internal heat, either through radioactive isotopes decay or tidal dissipation. Here, we quantify the impact of internal heating on stagnant-lid convection. We perform numerical simulations of convection combining strongly temperature-dependent viscosity and mixed (basal and internal) heating in 3D-Cartesian and spherical geometries, and use these simulations to build scaling laws relating surface heat flux, Φ_{surf}, interior temperature, T_m, and stagnant lid thickness, d_{lid}, to the Rayleigh number, heating rate, H, and top-to-bottom viscosity ratio, $\Delta\eta$. These relationships show that T_m increases with H but decreases with $\Delta\eta$, while Φ_{surf} increases with H and $\Delta\eta$. Importantly, they also describe heterogeneously heated systems well, provided that the maximum dissipation occurs in hottest regions. For H larger than a value H_{crit}, the bottom heat flux turns negative and the system cools down both at its top and bottom. Two additional interesting results are that (a) while the rigid lid stiffens (its mobility decreases) with increasing H, it also thins; and (b) H_{crit} increases with increasing $\Delta\eta$. We then use our scaling laws to assess the impact of tidal heating on Europa's ice shell properties and evolution. Our calculations suggest a shell thickness in the range 20–80 km, depending on viscosity and dissipated power, and show that internal heating has a stronger influence than the presence of impurities in the sub-surface ocean.

Plain Language Summary Convection is a mode of heat transfer that is thought to play or have played a key role in the cooling of planetary mantles and ice shells of icy bodies. The convection vigor, efficiency and ability to transport heat are all controlled by the properties of the systems in which it settles. In planetary mantles and ice shells, two important parameters are the variations of viscosity triggered by changes in temperature, which lead to the formation of a rigid lid at the top of the system, and the production of heat within the system, which weakens hot plumes rising from its base. In this article, we assess the combined effects of these two parameters. For this, we perform numerical simulations of convection, from which we deduce quantitative relationships between input and output parameters, the later including internal temperature and surface heat flux. We show that both heat flux and temperature increase with increasing internal heat production, while increasing the thermal viscosity contrast increases heat flux, but reduces temperature. We then apply our relationships to the case of Europa, a moon of Jupiter, and show that the thickness of its ice shell should be in the range 20–80 km.

1. Introduction

Heat transfer through planetary mantles and ice shells of large icy bodies is controlled by the properties of these systems. Due to the strong temperature-dependence of the viscosities of silicate rocks and ices, convection within rocky mantles and ice shells is likely to operate in the so-called stagnant-lid regime (e.g., Christensen, 1984; Moresi & Solomatov, 1995), unless, as in the case of the Earth, specific conditions allow the development of plate tectonics. In stagnant-lid convection, a rigid layer forms at the top of the system as an extension of the top thermal boundary layer (TBL). Because this layer is not mobile and transports heat by conduction, its presence strongly alters heat transfer. Another process altering the ability of convection to transfer heat toward the surface is the production of heat within the system. In systems heated both from their bases and their interiors, hot plumes rising from the bottom TBL get weaker with increasing rate of internal heating, and may not reach the surface if heat production is too high (e.g., Deschamps, Tackley, & Nakagawa, 2010; Travis & Olson, 1994). As a result, the amount of heat that can be extracted from regions located beneath is reduced. Ultimately, for rates of internal heating larger than a critical value, the

bottom heat flux turns negative, meaning that the system cools down both from its top and its base, while the region located beneath heats up. In the case of rocky planets, for instance, high heat production within the mantle would lead to a temporary increase of the core temperature and delay the cooling of the core, as more heat needs to be evacuated. Similarly, strong heat production in the outer ice shells of icy bodies would increase the subsurface ocean temperature, thinning the ice shell and delaying the crystallization of the ocean. In rocky planets, a source of internal heating is the decay of long-lived radio elements (^{235}U, ^{238}U, ^{232}Th, and ^{40}K). Short-lived elements, mainly ^{26}Al, mays have further played a role in the evolution of planetesimals, the parent bodies of rocky planets and asteroids. In the case of icy moons, tidal dissipation provides a source of heat within the ice shell or at its base. The amount of heat released, and thus the evolution of the body, depends on its orbital properties and may vary with time (e.g., Roberts & Nimmo, 2008; Tobie et al., 2003, 2005), with internal heating being negligible if the body is tidally locked or if it moves on a quasi-circular orbit. Quantifying the influence of internal heating on the ability of rocky mantles and ice shells to transport heat toward the surface is therefore essential to model accurately the long-term evolution of icy bodies and rocky planets.

A convenient way to quantify these effects is to build relationships (or scaling laws) between the key parameters describing thermal evolution (mainly interior temperature and surface heat flux) and the system properties, in particular its rheology, Rayleigh number (which measures the vigor of convection and depends itself on the system physical and thermal properties), and rate of internal heating. Scaling laws may be built from series of numerical simulations of convection, in which one or more parameters are systematically varied. Here, we conduct such a study in the case of mixed-heated systems animated by stagnant-lid convection. In addition to building scaling laws, we parameterize the value of internal heating at which the bottom heat flux turns negative. Finally, we use our results to model the properties and evolution of Europa's outer ice shell.

2. Numerical Model and Simulations

We performed numerical simulations of thermal convection for an incompressible (Boussinesq approximation), infinite Prandtl number fluid using StagYY (Tackley, 2008). The fluid is heated both from the bottom and from within, and internal heating is controlled by the heat production per unit of mass, H. The conservation equations of momentum, mass, and energy are then

$$\nabla \overline{\overline{\sigma}} - \nabla P = -\alpha \rho g T \boldsymbol{e}_z \tag{1}$$

$$\nabla \cdot \boldsymbol{v} = 0 \tag{2}$$

$$\text{and } \rho C_P \frac{\partial T}{\partial t} = k \nabla \cdot \left(\nabla T \right) - \rho C_P \boldsymbol{v} \cdot \nabla T + \rho H \tag{3}$$

where the elements of the deviatoric stress tensor, $\overline{\overline{\sigma}}$, are $\sigma_{ij} = \eta \left(\partial v_i / x_j + \partial v_j / x_i \right)$, P is the non-hydrostatic pressure, $\boldsymbol{v}$ is the velocity, T is the temperature, $\boldsymbol{e}_z$ is the radial unit vector, α, ρ, C_P, and k are the fluid thermal expansion coefficient, density, heat capacity, and thermal conductivity (all assumed constant throughout the system), g is the gravity acceleration, and η is the fluid viscosity, which here varies with temperature. Numerical methods used to solve Equations 1–3 are detailed in Tackley (2008).

The geometry is either 3D-Cartesian or 3D-spherical. In this later case, the spherical shell is modeled with two orthogonal grids called Yin and Yang stripes, which allow solving Equations 1–3 on a sphere without experiencing the numerical problems triggered by spherical coordinates around the polar axis (Kageyama & Sato, 2004). The shell curvature is controlled by the ratio between its inner and outer radii, $f = r_c / R$. Depending on the curvature and on the effective Rayleigh number, Ra_{eff} (defined below), we fix the resolution of each stripe between 192×576 and $512 \times 1{,}536$ (corresponding to spherical grids of 384×768 to $1{,}024 \times 2{,}048$ points), and the radial resolution of the shell between 96 and 192 points. 3D-Cartesian simulations are performed in boxes with a horizontal to vertical aspect ratio equal to 4 in both x and y directions, and a grid resolution of $128 \times 128 \times 64$ points for $Ra_{\text{eff}} < 10^6$, $256 \times 256 \times 128$ points for $10^6 \leq Ra_{\text{eff}} < 10^8$, and $384 \times 384 \times 192$ points for $Ra_{\text{eff}} \geq 10^8$. In addition, for both 3D-Cartesian and 3D-spherical cases, the grid is vertically refined at the top and at the bottom of the domain. Overall, this provides a good sampling of plumes and thermal boundary layers, when they exist. The top and bottom boundaries are free slip and isothermal, and reflective boundary conditions are imposed on sidewalls of 3D-Cartesian simulations. In

all cases, initial temperature distributions are built from random perturbations superposed on a 1D radial isotherm with thin TBLs at top and bottom.

Conservation equations are nondimensionalized with the characteristic properties of the system. Hereafter, nondimensional quantities are distinguished from their dimensional forms by adding a tilde, $\sim$. We used the thickness of the fluid layer, D, as characteristic length, and the temperature jump across this layer, ΔT, as characteristic temperature. The nondimensional temperature and internal heating rate are then given by $\tilde{T} = \left(T - T_{\text{surf}} \right)/\Delta T$, where T_{surf} is the surface temperature, and

$$\tilde{H} = \frac{\rho H D^2}{k \Delta T} \tag{4}$$

Nondimensionalization further implies to replace the source term of momentum equation, $\alpha \rho g T$, by the Rayleigh number,

$$Ra = \frac{\alpha \rho g \Delta T D^3}{\eta \kappa} \tag{5}$$

where $\kappa = k/\rho C_P$ is the thermal diffusivity. This number measures the ratio between buoyancy and viscous forces, and is an input parameter of our simulations.

The viscosity of ice strongly depends on temperature. Here, we modeled this dependency using the Frank-Kamenetskii (FK) approximation,

$$\eta = \eta_0 \exp\left[-a_\eta \frac{\left(T - T_0 \right)}{\Delta T} \right] \tag{6}$$

where η_0 and T_0 are the reference viscosity and temperature, and a_η a parameter that controls the amplitude of viscosity variations. This approximation overestimates the surface heat flux by up to 30% (e.g., Reese et al., 1999), and it does not account for dependencies of viscosity on strain rate and grain size. Nevertheless, it facilitates the calculations and allows capturing the role of one given specific parameter (here, internal heating), since a large number of FK simulations are available in the literature and can be used for comparisons. In the FK approximation, the nondimensional viscosity, $\tilde{\eta} = \eta/\eta_0$, is given as a function of the nondimensional temperature, $\tilde{T}$, by

$$\tilde{\eta} = \exp\left(-a_\eta \tilde{T} \right) \tag{7}$$

The top-to-bottom viscosity ratio, $\Delta \eta = \exp(a_\eta)$, is an input parameter of our simulations. For viscosity ratios larger than 10^4, convection generally operates in the so-called stagnant-lid regime (e.g., Christensen, 1984; Davaille & Jaupart, 1993; Moresi & Solomatov, 1995), in which a highly viscous and nearly motionless (stagnant) lid develops at the top of the fluid. In this layer, heat is transported by conduction, thus reducing the heat transfer. Experimental rheological laws for ice Ih (Durham et al., 2010) imply that the top-to-bottom viscosity ratios through the outer ice shells of icy bodies are much larger than 10^4. Convection within these shells, if occurring, should then operate in the stagnant-lid regime.

In most of our simulations internal heating is homogeneous, that is, H is constant throughout the system. Tidal dissipation within icy bodies may however depend on viscosity (Tobie et al., 2005), and thus vary with temperature. To assess the impact of this dependence on interior temperature and surface heat flux, we performed a few simulations in which internal heating depends on viscosity following (Roberts & Nimmo, 2008)

$$H = H_0 \left[\frac{\omega \eta/\mu}{1 + \left(\omega \eta/\mu \right)^2} \right] / \left[\frac{\omega \eta_{\text{ref}}/\mu}{1 + \left(\omega \eta_{\text{ref}}/\mu \right)^2} \right] \tag{8}$$

where η_{ref} and μ are the reference viscosity and rigidity of ice, H_0 a constant, and ω the orbital frequency given by $2\pi/P$, with P the orbital period. Equation 8 indicates that the maximum dissipation is obtained for a viscosity η such that the characteristic viscoelastic relaxation time, η/μ, is equal to $P/2\pi$. Note that the reference viscosity in Equation 8 may be different from that defined in Equation 6, provided that a correction is applied in calculations for consistency. Here, because we assumed that the strongest dissipation occurs close to the melting point of ice, η_{ref} is defined at the bottom of the ice shell (i.e., for $\tilde{T} = 1$). In Equation 6,

by contrast, the reference viscosity η_0 is the surface viscosity (for $\tilde{T} = 0$), which implies $\eta_{\text{ref}} = \eta_0 \exp(-a_\eta)$. The nondimensional internal heating rate may then be written

$$\tilde{H} = \tilde{H}_0 \left[\frac{\zeta_{\text{ref}} \tilde{\eta} \exp(a_\eta)}{1 + \left(\zeta_{\text{ref}} \tilde{\eta} \exp(a_\eta)\right)^2} \right] / \left[\frac{\zeta_{\text{ref}}}{1 + \zeta_{\text{ref}}^2} \right] \tag{9}$$

where $\zeta_{\text{ref}} = \omega \eta_{\text{ref}} / \mu$ and $\tilde{\eta}$ is given by Equation 7. The viscosity at which dissipation is maximal depends on the exact value of ζ_{ref}. Orbital periods of icy moons typically range from one to a few Earth's days, corresponding to ω in the range 4.0×10^{-6}–7.0×10^{-5} s^{-1}. Taking μ around 4.0×10^9 Pa and $10^{13} \leq \eta_{\text{ref}} \leq 10^{15}$ Pa s, corresponding to the viscosity of ice Ih close melting point (Montagnat & Duval, 2000), ζ_{ref} may be chosen in the range 10^{-2}–20. Here, we fixed ζ_{ref} to 1, so that the maximum dissipation occurs exactly at η_{ref}. This further implies that dissipation is strongest in hottest regions, including plumes heads, as done in Tobie et al. (2003). Generally speaking, it is interesting to note that for icy moons ζ_{ref} is fairly close to 1 (for instance, in the case of Europa, $P = 3.55$ Earth's days and taking $\eta_{\text{ref}} = 10^{14}$ Pa s one gets $\zeta_{\text{ref}} \sim 0.5$), meaning that the maximum dissipation should occur at temperatures close to the melting point of ice.

Because in our simulations viscosity varies throughout the system, the definition of the Rayleigh number, Ra (Equation 5), is ambiguous. The input Ra can however be defined at a specific viscosity (or, equivalently, a specific temperature), such that it does not vary during the simulations. Here, for convenience, we prescribed the surface Rayleigh number, Ra_{surf}, defined from the surface viscosity and temperature. In stagnant-lid convection, however, a better description of the vigor of convection beneath the lid is given by the effective Rayleigh number, Ra_{eff}, calculated with the viscosity at the temperature of the well-mixed interior (or interior temperature), $\tilde{T}_m$, defined as the volume averaged temperature within the well-mixed region. Following Equations 6 and 8, Ra_{eff} is given by

$$Ra_{\text{eff}} = Ra_{\text{surf}} \exp\left(a_\eta \tilde{T}_m\right) \tag{10}$$

Note that $\tilde{T}_m$, and thus Ra_{eff}, are outputs of the simulations.

A key output of the simulations is the amount of heat transported to the surface, measured with the surface heat flux. In mixed-heated systems, the conservation of energy implies that its top and bottom values, Φ_{top} and Φ_{bot}, satisfy

$$\Phi_{\text{top}} = f^2 \Phi_{\text{bot}} + \frac{\left(1 + f + f^2\right)}{3} H \tag{11}$$

where f is the ratio between the inner and outer shell radii, equal to 1 in Cartesian geometry. The characteristic heat flux is defined as the conductive heat flux for pure basal heating in Cartesian geometry, $\Phi_{\text{carac}} = k\Delta T / D$, such that the nondimensional form of Equation 11 is simply obtained by replacing each variable by its nondimensional equivalent, $\tilde{\Phi}_{\text{top}}$, $\tilde{\Phi}_{\text{bot}}$, and $\tilde{H}$. Equation 11 indicates that, for a given Φ_{top}, the production of heat within the system lowers the amount of heat that can be extracted from regions located below (for instance, planetary cores). If internal heating is too large, the system cannot extract heat from the bottom but cools down both from its top and its bottom (e.g., Moore, 2008; Vilella & Deschamps, 2018), meaning that Φ_{bot} is negative. To quantify this effect, it is useful to introduce the Urey ratio, measuring the ratio between the internal heat production and the surface heat flux,

$$Ur = \frac{\left(1 + f + f^2\right)}{3} \frac{H}{\Phi_{\text{top}}} \tag{12}$$

Equations 11 and 12 imply that $Ur > 1$ if Φ_{bot} is negative, and $0 \leq Ur \leq 1$ otherwise.

Convection operates only if the convective heat flux is larger than the conductive heat flux Φ_{cond}, which, for a mixed heated system, depends on depth (Table S1). Its surface expression is given by

$$\Phi_{\text{cond,top}} = f \frac{k\Delta T}{D} + \left(f + 2\right) \frac{\rho H D}{6} \tag{13}$$

whose nondimensional form (with respect to the characteristic heat flux) writes

$$\tilde{\Phi}_{\text{cond,top}} = f + \frac{\left(f + 2\right)}{6} \tilde{H} \tag{14}$$

The efficiency of heat transfer is measured with the Nusselt number, Nu, defined as the ratio between the convective and conductive heat flux. Therefore, convection operates if $Nu > 1$. As an example, in Cartesian geometry ($f = 1$), $Nu > 1$ requires that the surface nondimensional heat flux, $\tilde{\Phi}_{top}$, is larger than $\left(1 + \tilde{H}/2\right)$.

Using this setup, we performed 63 simulations in 3D-Cartesian geometry (including nine cases with heterogeneous heating) and 25 in 3D-spherical geometry (Table 1). For comparison, we also listed five cases with pure bottom heating taken from Deschamps and Lin (2014). Surface Rayleigh number, top-to-bottom viscosity ratio, and nondimensional heating rate are taken in the ranges $1 \leq Ra_{surf} \leq 180$, $10^4 \leq \Delta\eta \leq 10^8$, and $0.5 \leq \tilde{H} \leq 10$ respectively, leading to effective Rayleigh numbers between 2.0×10^5 and 2.0×10^8. In 3D-spherical cases, the inner-to-outer radii ratio is chosen between 0.6 and 0.85. For these ranges of values, the flow is time-dependent and reaches a quasi-stationary state (meaning that output properties, including $\tilde{T}_m$ and $\tilde{\Phi}_{top}$, oscillate around constant values) after some time. Output properties are estimated after the quasi-stationary phase has been reached, by time-averaging of each property over several oscillations.

3. Flow Pattern and Thermal Structure

3.1. Flow Pattern

Solomatov (1995) identified three different regimes under which convection in a temperature-dependent fluid may operate. Stagnant-lid convection appears for top-to-bottom viscosity ratios larger than 10^4 for Newtonian fluids (Moresi & Solomatov, 1995; Solomatov, 1995) and 10^8 for non-Newtonian fluids (Solomatov & Moresi, 1997), but it has also been suggested that for Newtonian fluids its occurrence requires larger viscosity contrasts as the Rayleigh number (Deschamps & Sotin, 2000) or shell curvature (Guerrero et al., 2018; Yao et al., 2014) increases. Stein et al. (2013) proposed two empirical criteria to assess the presence of a stagnant lid. First, a nondimensional surface velocity, $\tilde{v}_{surf}$, lower than 1; and second a mobility, M, defined as the ratio between $\tilde{v}_{surf}$ and the root mean square velocity of the whole system, smaller than 0.01. All our simulations satisfy these criteria (Table 1), and should thus belong to the stagnant-lid regime.

Figures 1–3 show snapshots of temperature fields and associated horizontally averaged profiles for 3D-Cartesian and 3D-spherical cases. 3D-Cartesian cases have identical surface Rayleigh number ($Ra_{surf} = 25$) and viscosity ratio ($\Delta\eta = 10^6$), but different rates of internal heating. 3D-spherical cases are obtained with $f = 0.6$, $Ra_{surf} = 16$, $\Delta\eta = 10^6$ and, again, different values of $\tilde{H}$. A stagnant lid is clearly visible in all cases. A closer examination (Section 3.2) indicates that the lid is thinning with increasing $\tilde{H}$. Internal heating has a strong impact on the flow structure beneath the lid. With increasing $\tilde{H}$, we observe a trend similar to that reported for isoviscous fluids (e.g., Deschamps, Tackley, & Nakagawa, 2010; Travis & Olson, 1994). Plumes are getting thinner, more diffuse and may not reach the bottom of the stagnant lid, indicating that the growth of hot instabilities in the basal thermal boundary layer (TBL) is more difficult. The flow is progressively controlled by downwellings and return flow. Importantly, if $\tilde{H}$ is large enough (Figures 1g, 1h, 2c and 2d), the bottom TBL disappears and the heat flux turns negative (Figures 3d and 3f). The system then cools down both at its top and its bottom, and the Urey ratio (Equation 12) is larger than 1.

3.2. Properties of the Stagnant Lid

We measured the (nondimensional) thickness of the stagnant lid, $\tilde{d}_{lid}$, using the method developed by Davaille and Jaupart (1993), in which the base of the stagnant lid is defined by the intersection between the tangent at the point of inflexion of the horizontally averaged profile of vertically advected heat, $\tilde{v}_z\tilde{T}$, with the origin axis ($\tilde{v}_z\tilde{T} = 0$; left plots in Figure 3). The values of $\tilde{d}_{lid}$ we obtained are reported in Table 1. All other parameters being equal, $\tilde{d}_{lid}$ decreases with increasing rate of internal heating, while both $\tilde{v}_{surf}$ and M are decreasing. Increasing internal heating thus results in thinner but stiffer (less mobile) stagnant lids.

Because heat is transported by conduction in the stagnant lid, it is possible to derive analytical expressions for the horizontally averaged temperature in this region by solving the conduction heat equation. Assuming that internal heating rate and density are constant and that the surface temperature and heat flux (T_{surf} and Φ_{surf}) are known, the (dimensional) temperature profile is given either by Equation S7 in Cartesian geometry, or Equation S8 in spherical geometry (Supporting Information S1). Note that these expressions are independent of the lid thickness. Their nondimensional forms are

Table 1
Simulations of Stagnant-Lid Convection With Mixed Heating

Ra_{surf}	f	$\Delta\eta$	$\tilde{H}$	$\tilde{H}_0$	Grid size	$\tilde{T}_m$	$\tilde{\Phi}_{\text{top}}$	$\tilde{\Phi}_{\text{bot}}$	Ur	$\text{rms}(\tilde{v})$	$\tilde{v}_{\text{surf}}$	Ra_{eff}	$\tilde{d}_{\text{lid}}$	$\tilde{T}_{\text{lid}}$
3D-Cartesian														
16.0	-	10^4	4.0		$128 \times 128 \times 64$	1.075	3.458	−0.543	1.16	26.9	1.2×10^{-1}	3.19×10^5	0.316	0.892
32.0	-	10^4	2.0		$128 \times 128 \times 64$	0.969	2.836	0.837	0.71	40.6	3.8×10^{-1}	2.40×10^5	0.324	0.814
32.0	-	10^4	3.0		$128 \times 128 \times 64$	1.016	3.222	0.223	0.93	39.9	2.9×10^{-1}	3.71×10^5	0.302	0.835
32.0	-	10^4	4.0		$128 \times 128 \times 64$	1.051	3.678	−0.323	1.09	41.3	2.2×10^{-1}	5.12×10^5	0.280	0.872
75.0	-	10^4	1.5		$128 \times 128 \times 64$	0.937	3.202	1.702	0.47	76.9	1.01	4.21×10^5	0.268	0.804
75.0	-	10^4	3.0		$128 \times 128 \times 64$	0.998	3.668	0.670	0.82	69.7	5.4×10^{-1}	7.36×10^5	0.249	0.820
75.0	-	10^4	5.0		$256 \times 256 \times 128$	1.059	4.577	−0.422	1.09	73.4	2.5×10^{-1}	1.05×10^6	0.221	0.889
17.9	-	3.2×10^4	2.0		$128 \times 128 \times 64$	0.977	2.887	0.887	0.69	52.1	1.3×10^{-1}	4.51×10^5	0.323	0.828
17.9	-	3.2×10^4	4.0		$128 \times 128 \times 64$	1.042	3.740	−0.260	1.07	53.5	8.2×10^{-2}	8.85×10^5	0.276	0.880
55.9	-	3.2×10^4	0.0		$128 \times 128 \times 64$	0.874	3.000	3.001	0.00	112.5	7.1×10^{-1}	4.84×10^5	0.254	0.762
55.9	-	3.2×10^4	1.0		$128 \times 128 \times 64$	0.922	3.374	2.376	0.30	120.7	5.6×10^{-1}	7.92×10^5	0.252	0.818
55.9	-	3.2×10^4	2.0		$256 \times 256 \times 128$	0.962	3.649	1.649	0.55	117.4	2.6×10^{-1}	1.21×10^6	0.249	0.847
55.9	-	3.2×10^4	3.0		$256 \times 256 \times 128$	0.990	3.959	0.959	0.76	104.8	2.0×10^{-1}	1.62×10^6	0.233	0.840
55.9	-	3.2×10^4	6.0		$256 \times 256 \times 128$	1.069	5.352	−0.648	1.12	116.2	1.3×10^{-2}	3.65×10^6	0.192	0.917
178.9	-	3.2×10^4	4.0		$256 \times 256 \times 128$	0.985	5.344	1.343	0.75	198.9	5.4×10^{-1}	4.92×10^6	0.168	0.843
10.0	-	10^5	2.0		$128 \times 128 \times 64$	0.975	2.976	0.977	0.67	69.7	5.7×10^{-1}	7.62×10^5	0.319	0.849
10.0	-	10^5	4.0		$256 \times 256 \times 128$	1.034	3.818	−0.181	1.05	69.1	4.1×10^{-2}	1.38×10^6	0.273	0.894
10.0	-	10^5	6.0		$256 \times 256 \times 128$	1.110	5.007	−0.994	1.20	96.4	2.4×10^{-1}	3.60×10^6	0.224	0.971
31.6	-	10^5	0.0		$256 \times 256 \times 128$	0.891	3.143	3.144	0.00	148.1	3.0×10^{-1}	9.06×10^5	0.257	0.809
31.6	-	10^5	0.492	1.0	$256 \times 256 \times 128$	0.915	3.276	2.785	0.15	156.4	2.4×10^{-1}	1.18×10^6	0.257	0.842
31.6	-	10^5	2.0		$256 \times 256 \times 128$	0.964	3.772	1.774	0.53	148.2	1.2×10^{-1}	2.08×10^6	0.244	0.860
31.6	-	10^5	2.096	3.0	$256 \times 256 \times 128$	0.982	3.493	1.397	0.60	132.2	7.2×10^{-2}	2.57×10^6	0.246	0.858
31.6	-	10^5	4.0		$256 \times 256 \times 128$	1.006	4.471	0.471	0.89	132.6	7.3×10^{-2}	3.38×10^6	0.214	0.866
31.6	-	10^5	5.0		$256 \times 256 \times 128$	1.028	4.898	−0.101	1.02	133.7	7.2×10^{-2}	4.35×10^6	0.202	0.889
31.6	-	10^5	6.0		$256 \times 256 \times 128$	1.054	5.447	−0.553	1.10	145.7	6.6×10^{-2}	5.88×10^6	0.187	0.915
50.6	-	10^5	2.0		$256 \times 256 \times 128$	0.957	4.236	2.236	0.47	195.8	1.5×10^{-1}	3.08×10^6	0.214	0.861
50.6	-	10^5	3.0		$256 \times 256 \times 128$	0.979	4.501	1.502	0.67	169.1	1.3×10^{-1}	3.97×10^6	0.201	0.843
50.6	-	10^5	3.022	4.0	$256 \times 256 \times 128$	0.991	4.182	1.159	0.72	170.4	8.9×10^{-2}	4.58×10^6	0.206	0.860
50.6	-	10^5	6.0		$256 \times 256 \times 128$	1.035	5.710	−0.290	1.05	179.8	1.1×10^{-1}	7.60×10^6	0.174	0.900
50.6	-	10^5	8.0		$256 \times 256 \times 128$	1.089	6.970	−1.029	1.15	226.5	7.9×10^{-2}	1.41×10^7	0.149	0.952
50.6	-	10^5	10.0		$256 \times 256 \times 128$	1.145	8.427	−1.573	1.19	313.9	6.7×10^{-2}	2.70×10^7	0.129	1.007
56.6	-	3.2×10^5	4.0		$256 \times 256 \times 128$	0.980	5.685	1.685	0.70	326.6	9.4×10^{-2}	1.41×10^7	0.161	0.864
56.6	-	3.2×10^5	8.0		$256 \times 256 \times 128$	1.040	7.461	−0.539	1.07	354.8	7.4×10^{-2}	2.99×10^7	0.132	0.914
113.1	-	3.2×10^5	4.0		$256 \times 256 \times 128$	0.970	6.600	2.602	0.61	486.3	2.3×10^{-1}	2.48×10^7	0.137	0.867
10.0	-	10^6	1.0		$256 \times 256 \times 128$	0.940	3.913	2.914	0.31	266.4	4.0×10^{-2}	4.38×10^6	0.232	0.880
10.0	-	10^6	2.0		$256 \times 256 \times 128$	0.963	4.162	2.164	0.48	240.1	2.7×10^{-2}	5.97×10^6	0.227	0.894
10.0	-	10^6	3.0		$256 \times 256 \times 128$	0.981	4.455	1.456	0.67	213.7	2.1×10^{-2}	7.74×10^6	0.209	0.865
10.0	-	10^6	4.0		$256 \times 256 \times 128$	0.995	4.755	0.754	0.84	216.69	1.5×10^{-2}	9.33×10^6	0.203	0.882
10.0	-	10^6	4.251	5.5	$256 \times 256 \times 128$	1.012	4.442	0.192	0.96	216.81	1.7×10^{-2}	1.18×10^7	0.205	0.912
10.0	-	10^6	5.0		$256 \times 256 \times 128$	1.010	5.179	0.178	0.97	217.0	1.8×10^{-1}	1.15×10^7	0.190	0.895
10.0	-	10^6	6.0		$256 \times 256 \times 128$	1.030	5.689	−0.312	1.05	227.3	1.5×10^{-1}	1.51×10^7	0.177	0.915

Table 1
Continued

Ra_{surf}	f	$\Delta\eta$	$\tilde{H}$	$\tilde{H}_0$	Grid size	$\tilde{T}_m$	$\tilde{\Phi}_{\text{top}}$	$\tilde{\Phi}_{\text{bot}}$	Ur	$\text{rms}(\tilde{v})$	$\tilde{v}_{\text{surf}}$	Ra_{eff}	$\tilde{d}_{\text{lid}}$	$\tilde{T}_{\text{lid}}$
10.0	-	10^6	8.0		$256 \times 256 \times 128$	1.082	7.007	−0.994	1.14	308.3	1.4×10^{-1}	3.11×10^7	0.150	0.963
25.0	-	10^6	0.0		$256 \times 256 \times 128$	0.912	4.415	4.416	0.00	456.1	2.8×10^{-1}	7.38×10^6	0.193	0.850
25.0	-	10^6	2.0		$256 \times 256 \times 128$	0.952	5.234	3.235	0.38	371.5	3.8×10^{-2}	1.29×10^7	0.171	0.868
25.0	-	10^6	2.059	3.0	$256 \times 256 \times 128$	0.959	4.984	2.926	0.41	370.8	4.5×10^{-2}	1.42×10^7	0.179	0.892
25.0	-	10^6	3.0		$256 \times 256 \times 128$	0.969	5.426	2.428	0.55	367.6	2.2×10^{-2}	1.63×10^7	0.169	0.873
25.0	-	10^6	3.041	4.0	$256 \times 256 \times 128$	0.977	5.059	2.016	0.60	355.2	3.3×10^{-2}	1.82×10^7	0.176	0.892
25.0	-	10^6	4.0		$256 \times 256 \times 128$	0.981	5.639	1.637	0.71	361.3	4.3×10^{-2}	1.92×10^7	0.165	0.876
25.0	-	10^6	4.929	6.0	$256 \times 256 \times 128$	1.001	5.564	0.635	0.89	361.2	4.6×10^{-2}	2.54×10^7	0.163	0.905
25.0	-	10^6	6.0		$256 \times 256 \times 128$	1.006	6.392	0.394	0.94	366.8	3.6×10^{-2}	2.71×10^7	0.150	0.889
25.0	-	10^6	8.0		$256 \times 256 \times 128$	1.037	7.450	−0.550	1.07	403.1	3.3×10^{-2}	4.14×10^7	0.133	0.922
45.0	-	10^6	4.0		$256 \times 256 \times 128$	0.973	6.377	2.380	0.63	515.9	8.5×10^{-2}	3.10×10^7	0.144	0.875
5.6	-	3.2×10^6	4.0		$256 \times 256 \times 128$	0.992	4.957	0.956	0.81	281.6	1.1×10^{-1}	1.57×10^7	0.194	0.886
5.6	-	3.2×10^6	8.0		$256 \times 256 \times 128$	1.065	7.130	−0.870	1.12	377.2	7.4×10^{-2}	4.71×10^7	0.146	0.958
41.9	-	3.2×10^6	4.0		$256 \times 256 \times 128$	0.967	7.495	3.496	0.53	937.6	5.4×10^{-2}	8.18×10^7	0.123	0.892
10.0	-	10^7	0.0		$256 \times 256 \times 128$	0.923	5.271	5.278	0.00	964.4	8.9×10^{-2}	2.94×10^7	0.165	0.869
10.0	-	10^7	2.948	4.0	$256 \times 256 \times 128$	0.969	6.089	3.142	0.48	753.1	1.9×10^{-2}	6.14×10^7	0.152	0.926
10.0	-	10^7	4.0		$256 \times 256 \times 128$	0.975	6.568	2.571	0.61	732.8	1.5×10^{-2}	6.76×10^7	0.149	0.935
10.0	-	10^7	8.0		$384 \times 384 \times 192$	0.940	8.115	0.114	0.99	734.9	1.1×10^{-2}	1.15×10^8	0.121	0.920
10.0	-	10^7	10.0		$384 \times 384 \times 192$	1.035	9.325	−0.676	1.07	851.5	1.0×10^{-2}	1.79×10^8	0.108	0.948
3.2	-	10^8	0.0		$384 \times 384 \times 192$	0.934	6.000	5.999	0.00	1,228.2	2.0×10^{-2}	9.46×10^7	0.147	0.885
3.2	-	10^8	2.871	4.0	$384 \times 384 \times 192$	0.967	6.857	3.986	0.42	1,353.7	4.8×10^{-3}	1.74×10^8	0.137	0.941
3.2	-	10^8	4.0		$384 \times 384 \times 192$	0.971	7.403	3.401	0.54	1,328.9	4.0×10^{-3}	1.88×10^8	0.127	0.909
Spherical														
16.0	0.60	10^6	4.0		$192 \times 576 \times 96 \times 2$	0.932	3.970	3.767	0.67	242.7	8.0×10^{-2}	6.25×10^6	0.221	0.859
16.0	0.60	10^6	10.0		$192 \times 576 \times 128 \times 2$	1.034	6.313	−0.607	1.03	307.6	2.2×10^{-2}	2.55×10^7	0.155	0.918
5.1	0.60	10^7	4.0		$192 \times 576 \times 128 \times 2$	0.929	4.389	4.928	0.60	396.0	2.1×10^{-2}	1.64×10^7	0.204	0.887
10.0	0.70	10^6	8.0		$192 \times 576 \times 96 \times 2$	0.964	3.964	2.129	0.74	193.4	3.5×10^{-2}	6.12×10^6	0.228	0.861
10.0	0.70	10^6	8.0		$256 \times 768 \times 128 \times 2$	1.035	5.596	−0.498	1.04	234.5	1.7×10^{-2}	1.61×10^7	0.177	0.918
3.2	0.70	10^7	8.0		$256 \times 768 \times 128 \times 2$	1.011	5.833	−0.011	1.00	366.1	4.4×10^{-2}	3.78×10^7	0.167	0.908
10.0	0.70	10^7	2.0		$192 \times 576 \times 128 \times 2$	0.907	4.914	7.046	0.30	622.9	6.1×10^{-2}	2.23×10^7	0.171	0.854
15.8	0.70	10^7	3.0		$192 \times 576 \times 128 \times 2$	0.917	5.845	7.461	0.37	797.0	5.8×10^{-2}	4.15×10^7	0.149	0.879
3.2	0.75	10^7	4.0		$256 \times 768 \times 128 \times 2$	0.964	4.530	2.568	0.68	346.0	9.2×10^{-2}	1.78×10^7	0.206	0.894
3.2	0.75	10^7	8.0		$256 \times 768 \times 128 \times 2$	1.017	6.049	−0.208	1.02	378.8	4.2×10^{-2}	4.19×10^7	0.162	0.915
3.2	0.75	10^7	10.0		$256 \times 768 \times 128 \times 2$	1.054	7.188	−0.923	1.07	496.3	3.5×10^{-2}	7.49×10^7	0.141	0.950
10.0	0.75	10^7	4.0		$256 \times 768 \times 128 \times 2$	0.945	5.834	4.883	0.53	660.7	2.0×10^{-2}	4.19×10^7	0.155	0.892
10.0	0.75	10^7	10.0		$384 \times 1152 \times 192 \times 2$	1.005	7.817	0.192	0.99	716.3	9.1×10^{-3}	1.10×10^8	0.123	0.912
10.0	0.80	10^6	2.0		$256 \times 768 \times 96 \times 2$	0.938	3.617	3.107	0.45	223.4	7.4×10^{-2}	4.25×10^6	0.242	0.859
10.0	0.80	10^6	4.0		$256 \times 768 \times 96 \times 2$	0.977	4.267	1.580	0.76	192.0	3.0×10^{-2}	7.18×10^6	0.213	0.857
10.0	0.80	10^6	8.0		$256 \times 768 \times 128 \times 2$	1.051	6.039	−0.729	1.08	258.1	1.6×10^{-2}	2.02×10^7	0.168	0.931
10.0	0.80	10^6	10.0		$256 \times 768 \times 128 \times 2$	1.098	7.289	−1.315	1.12	366.4	1.3×10^{-2}	3.89×10^7	0.144	0.978
32.0	0.80	10^6	4.0		$256 \times 768 \times 128 \times 2$	0.952	5.412	3.368	0.60	404.7	1.7×10^{-1}	1.65×10^7	0.167	0.879
3.2	0.80	10^7	4.0		$256 \times 768 \times 128 \times 2$	0.972	4.666	2.205	0.70	359.2	1.1×10^{-2}	2.02×10^7	0.201	0.893

Table 1
Continued

Ra_{surf}	f	$\Delta\eta$	$\tilde{H}$	$\tilde{H}_0$	Grid size	$\tilde{T}_m$	$\tilde{\Phi}_{top}$	$\tilde{\Phi}_{bot}$	Ur	rms$(\tilde{v})$	$\tilde{v}_{surf}$	Ra_{eff}	$\tilde{d}_{lid}$	$\tilde{T}_{lid}$
3.2	0.80	10^7	8.0		$256 \times 768 \times 128 \times 2$	1.025	6.253	−0.395	1.04	401.8	3.8×10^{-3}	4.69×10^7	0.159	0.922
3.2	0.80	10^7	10.0		$256 \times 768 \times 128 \times 2$	1.058	7.503	−0.979	1.08	557.2	4.6×10^{-3}	7.99×10^7	0.134	0.951
1.0	0.80	10^8	4.0		$512 \times 1536 \times 192 \times 2$	0.966	5.266	3.157	0.62	626.5	2.5×10^{-3}	5.32×10^7	0.181	0.920
3.2	0.80	10^8	3.0		$512 \times 1536 \times 192 \times 2$	0.940	6.482	6.387	0.38	1,250.1	1.1×10^{-2}	1.11×10^8	0.144	0.930
10.0	0.85	10^6	4.0		$256 \times 768 \times 128 \times 2$	0.983	4.403	1.345	0.78	201.5	2.6×10^{-2}	7.86×10^6	0.215	0.883
10.0	0.85	10^6	8.0		$256 \times 768 \times 128 \times 2$	1.058	6.253	−0.838	1.10	283.1	1.4×10^{-2}	2.23×10^7	0.164	0.940

Note. Listed parameters are the surface Rayleigh number, Ra_{surf}, the inner-to-outer radii ratio (for spherical cases), f, the top-to-bottom thermal viscosity ratio, $\Delta\eta$, the nondimensional rate of internal heating, $\tilde{H}$, the constant $\tilde{H}_0$ (for heterogeneous internal heating cases, Equation 9), the grid size, the average nondimensional temperature of the well-mixed interior, $\tilde{T}_m$, the top and bottom nondimensional heat fluxes, $\tilde{\Phi}_{top}$ and $\tilde{\Phi}_{bot}$, the Urey ratio, Ur (Equation 12), the root mean square velocity of the whole system, rms$(\tilde{v})$, the average surface velocity, $\tilde{v}_{surf}$, the effective Rayleigh number, Ra_{eff} (Equation 10), the nondimensional thickness of the stagnant lid, $\tilde{d}_{lid}$, calculated following the method of Davaille and Jaupart (1993), and the temperature at the base of this lid, $\tilde{T}_{lid}$, deduced from Equations 19 or 20 with observed values of $\tilde{\Phi}_{top}$ and d_{lid}. Calculations with pure bottom heating ($\tilde{H} = 0$) are taken from Deschamps and Lin (2014).

$$\left\langle \tilde{T} \right\rangle = \tilde{z}\tilde{\Phi}_{top} - \frac{\tilde{H}}{2}\tilde{z}^2 \tag{15}$$

where $\tilde{z}$ is the nondimensional depth, and

$$\left\langle \tilde{T} \right\rangle = -\frac{\tilde{\Phi}_{top}}{(1-f)}\left[1 - \frac{\tilde{R}}{\tilde{r}}\right] + \frac{\tilde{H}}{6(1-f)^2}\left[2\left(1 - \frac{\tilde{R}}{\tilde{r}}\right) + \left(1 - \frac{\tilde{r}^2}{\tilde{R}^2}\right)\right] \tag{16}$$

where $\tilde{r} = (1-f)^{-1} - \tilde{z}$ and $\tilde{R} = (1-f)^{-1}$ are the nondimensional radius and total radius, respectively. Equations 15 and 16 provide an excellent description of the top part of the horizontally averaged temperature profiles, corresponding to the stagnant lid (dashed dark red curves in Figure 3). Equation 15 implies that temperature profile in the stagnant lid have a downward curvature. This curvature is not much pronounced, but insets in Figure 3 clearly show that the temperature profile deviates from a linear increase (dashed black lines in insets), and thus satisfy this condition. Solving heat equation for viscosity-dependent internal heating is generally more complex. In our case, however, imposing the maximum dissipation at lowest viscosity implies that dissipation in the lid is close to zero. A good description of the temperature profile within the lid is then obtained by setting $\tilde{H} = 0$ in Equations 15 and 16.

The horizontally averaged heat flux within the stagnant lid is given by Equations S11 and S12, whose nondimensional versions are

$$\tilde{\Phi}(\tilde{z}) = \frac{\tilde{T}_{lid}}{\tilde{d}_{lid}} + \frac{\tilde{H}}{2}\left(\tilde{d}_{lid} - 2\tilde{z}\right) \tag{17}$$

and

$$\tilde{\Phi}(\tilde{r}) = \frac{\tilde{T}_{lid}}{\tilde{d}_{lid}}f_{lid}\frac{\tilde{R}^2}{\tilde{r}^2} - \frac{\tilde{H}}{6(1-f)}\left[f_{lid}(1 + f_{lid})\frac{\tilde{R}^2}{\tilde{r}^2} - 2\frac{\tilde{r}}{\tilde{R}}\right], \tag{18}$$

where $\tilde{d}_{lid}$ and $\tilde{T}_{lid}$ are the nondimensional stagnant lid thickness and basal temperature, respectively, and $f_{lid} = (R - d_{lid})/R = 1 - (1-f)d_{lid}/D$ is the ratio between the radius of its base and the total radius. To obtain Equation 18, it is useful to recall that $\tilde{R} = (1-f)^{-1}$. Equations 17 and 18 can be used to estimate the temperature at the bottom of the lid as a function of the surface heat flux and stagnant lid thickness. Setting $\tilde{z} = 0$ in Equation 17 and $\tilde{r} = \tilde{R}$ in Equation 18, and re-arranging the terms leads to

$$\tilde{T}_{lid} = \tilde{d}_{lid}\left(\tilde{\Phi}_{top} - \frac{1}{2}\tilde{H}\tilde{d}_{lid}\right) \tag{19}$$

in Cartesian geometry, and

$$\tilde{T}_{lid} = \frac{\tilde{d}_{lid}}{f_{lid}}\left[\tilde{\Phi}_{top} - \frac{1}{6}\tilde{H}\frac{\left(2 - f_{lid} - f_{lid}^2\right)}{(1-f)}\right] \tag{20}$$
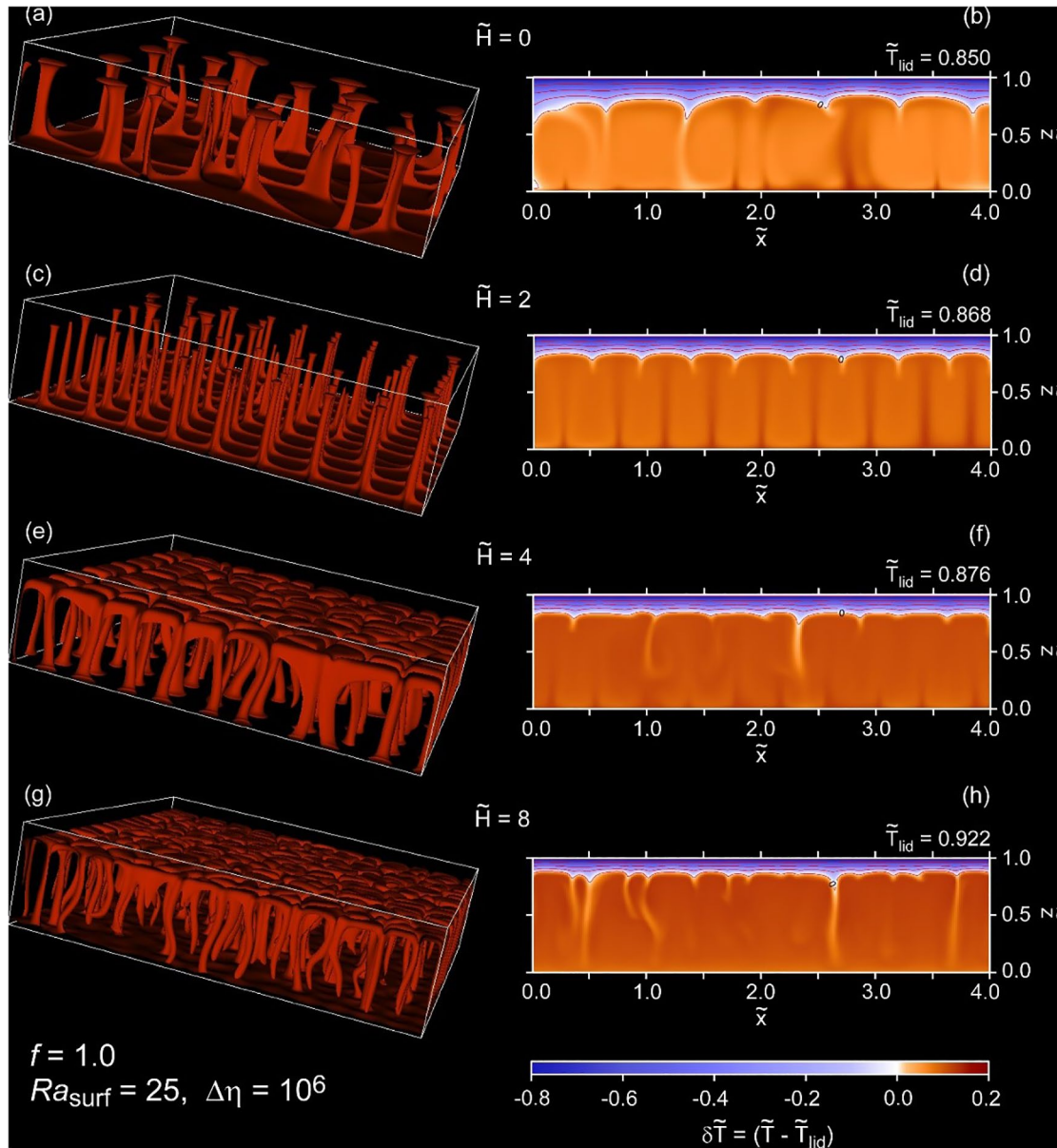
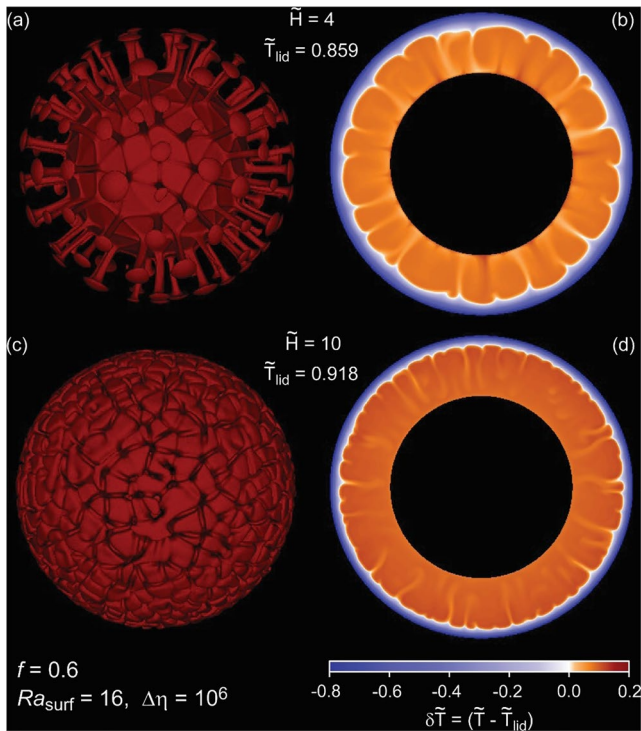**Figure 1.** Snapshots of the temperature field (left) and vertical slices of the residual temperature relative to the temperature at the bottom of the stagnant lid $\tilde{T}_{lid}$ (right) for cases with surface Rayleigh number $Ra_{surf} = 25$, thermal viscosity ratio $\Delta\eta = 10^6$ and different values of the nondimensional rate of internal heating, $\tilde{H}$. (a–b) $\tilde{H} = 0$ (pure bottom heating), (c–d) $\tilde{H} = 2$, (e–f) $\tilde{H} = 4$, and (g–h) $\tilde{H} = 8$. Isosurface values are (a) $\tilde{T} = 0.95$, (c) $\tilde{T} = 0.97$, (e) $\tilde{T} = 0.95$, and (g) $\tilde{T} = 1.015$. In the case with $\tilde{H} = 8$ (plots g–h) the bottom heat flux is negative, that is, the system cools down both at its top and its bottom. Value of $\tilde{T}_{lid}$ are indicated on each panel.

in spherical geometry. Values of $\tilde{T}_{lid}$ deduced either from Equations 19 or 20 are reported in Table 1. Note that the values of $\tilde{T}_{lid}$ calculated with Equations 19 or 20 are slightly larger than that measured on the horizontally averaged profiles of temperature.

4. Scaling Laws

Estimating the thermal evolutions of planets and satellites with parameterized convection methods requires the knowledge of appropriate relationships, or scaling laws, between input parameters (Rayleigh number, viscosity ratio, and rate of internal heating) and observables (interior temperature, surface heat

Figure 2. Isosurface of the temperature (left) and polar slices of the residual temperature relative to the temperature at the bottom of the stagnant lid $\tilde{T}_{lid}$ (right) for snapshots of two cases in 3D-spherical geometry with $f = 0.6$, surface Rayleigh number $Ra_{surf} = 16$, thermal viscosity ratio $\Delta\eta = 10^6$ and two values of the nondimensional rate of internal heating, $\tilde{H} = 4$, (a–b) and $\tilde{H} = 10$ (c–d). Isosurface values are $\tilde{T} = 0.95$ in plot (a) and $\tilde{T} = 1.03$ in plot (c). In the case with $\tilde{H} = 10$ (plots c–d), the bottom heat flux is negative, that is, the system cools down both at its top and its bottom. Value of $\tilde{T}_{lid}$ are indicated on each panel.

flux, stagnant lid thickness). For bottom heated stagnant-lid convection, scaling laws have been built in different geometries (Deschamps & Lin, 2014; Moresi & Solomatov, 1995; Solomatov, 1995; Yao et al., 2014). Reese et al. (1999) further derived scaling laws for stagnant-lid convection in a purely internally heated fluid, and found that this scaling is very similar to that obtained by Solomatov (1995) for a bottom heated fluid in 2D-Cartesian geometry. Results from our numerical simulations allow us to go a step further by building scaling laws for mixed-heated stagnant-lid convection. These are detailed below and summarized in Table 2.

4.1. Temperature of the Well-Mixed Interior

Numerical simulations indicate that the interior temperature of an iso-viscous, mixed-heated fluid is well described by a relationship combining the interior temperature for pure bottom and pure internal heating (Deschamps, Tackley, & Nakagawa, 2010; Sotin & Labrosse, 1999). Here, we followed a similar approach and built a scaling that combines the interior temperature for a bottom-heated fluid animated by stagnant-lid convection (Deschamps & Lin, 2014; Yao et al., 2014), and for an internally heated fluid, leading to

$$\tilde{T}_m = 1 - \frac{a_1}{f^{a_2}\gamma} + \left(c_1 + c_2 f\right)\left[\frac{\left(1 + f + f^2\right)}{3}\tilde{H}\right]^{c_4}\frac{1}{Ra_{eff}^{c_3}} \quad (21)$$

where parameters a_1, a_2 and c_1 to c_4 can be obtained by inversion of the $\tilde{T}_m$ obtained by our simulations (Table 1), and $\gamma = \Delta T / \Delta T_v$ is the nondimensional inverse of the viscous temperature scale, ΔT_v, defined as

$$\Delta T_v = \left(-\frac{1}{\eta}\frac{d\eta}{dT}|_{T=T_m}\right)^{-1} \quad (22)$$

In the case of Frank-Kamenetskii approximation (Equation 6), $\gamma = a_\eta = \ln(\Delta\eta)$. For consistency with scaling laws obtained for pure bottom heating, we fixed a_1 and a_2 to the values obtained by Yao et al. (2014), that is, $a_1 = 1.23$ and $a_2 = 1.5$. We then performed two separate inversions, for $Ur < 1$ and $Ur > 1$, in which we excluded simulations with heterogeneous heating. The inversion method follows the generalized inversion method of Tarantola and Valette (1982), and we assumed relative uncertainties of 0.5% on observed $\tilde{T}_m$, accounting for its time-variations during the steady-state phase. For $Ur < 1$, the best fitting values are $c_1 = 4.3$, $c_2 = -2.8$, $c_3 = 0.26$, and $c_4 = 0.96$, with a chi-square of 20 (the total number of experiments used for this inversion being 46). The value of c_3 is fairly close to the theoretical value of the Rayleigh number exponent for a purely internally heated fluid, 0.25 (Parmentier & Sotin, 2000). We therefore did an additional inversion in which we fixed c_3 to 0.25, and (for simplicity) c_4 to 1.0, and found $c_1 = 3.5 \pm 0.12$ and $c_2 = -2.3 \pm 0.11$, still with a good chi-square, around 30. We followed a similar procedure for $Ur > 1$ (28 simulations). In that case, the best fit is obtained for $c_1 = 4.5$, $c_2 = -3.1$, $c_3 = 0.34$, and $c_4 = 1.75$. Fixing, for simplicity, c_3 to 1/3, we obtained $c_1 = 4.4 \pm 0.22$, $c_2 = -3.0 \pm 0.17$, and $c_4 = 1.72 \pm 0.02$, with a chi-square of 39. Figure 4a compares modeled and observed values of $\tilde{T}_m$. Note that the calculations with heterogeneous heating, which were all conducted with $Ur < 1$, are well described by the scaling law for $Ur < 1$, even though they were not included in the inversion process.

Because the effective Rayleigh number, Ra_{eff}, depends on $\tilde{T}_m$, solving Equation 21 for $\tilde{T}_m$ requires the use of a zero-search method. As a consequence, identifying trends in the variations of $\tilde{T}_m$ with the input model parameters (surface Rayleigh number, rate of internal heating, thermal viscosity ratio, and curvature) is not straightforward. However, a close examination of Table 1 indicates that, other parameters being fixed, $\tilde{T}_m$ increases with $\tilde{H}$ and f, but decreases with Ra_{surf}. Changes of $\tilde{T}_m$ with $\Delta\eta$ are more complex (Figure S2a). For $\tilde{H}$ around 0.5–1.0 and higher, $\tilde{T}_m$ first decreases with increasing $\Delta\eta$, reaches a minimum for a value of
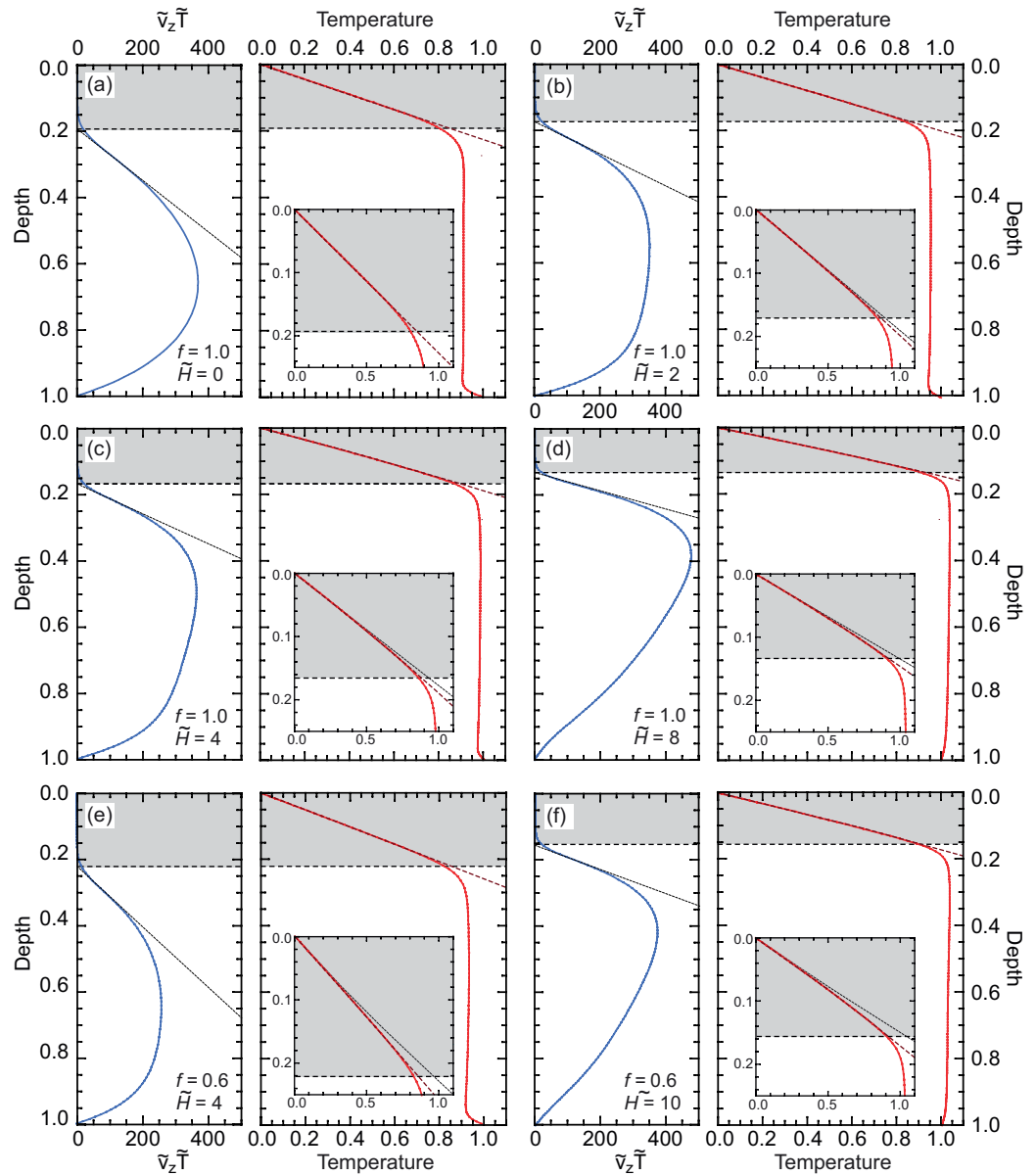
Figure 3. Horizontally averaged profiles of temperature (right plot in each panel) and vertically advected heat flow (left plot) for four cases in 3D-Cartesian geometry (plots a–d) and two cases in 3D-spherical geometry with inner-to-outer radii ratio $f = 0.6$ (plots e–f). Surface Rayleigh number, Ra_{surf}, is equal to 25 for the 3D-Cartesian cases and 16 for the spherical cases, and the top-to-bottom viscosity ratio is $\Delta\eta = 10^6$ in all cases. Heating is uniform, and the nondimensional heating rate is (a) $\tilde{H} = 0$, (b) $\tilde{H} = 2$, (c) $\tilde{H} = 4$, (d) $\tilde{H} = 8$, (e) $\tilde{H} = 4$, (f) $\tilde{H} = 10$. The gray areas denote the vertical extension of the stagnant lid. The dashed lines in the plots of advected heat flow show the tangent to the point of inflexion, whose intersection with the origin axis defines the bottom of the lid. The dashed dark-red curves in the plots of temperature are determined assuming a conductive temperature profile in the stagnant lid, and are calculated following either $\tilde{T}(\tilde{z}) = \tilde{T}_{lid}\tilde{z}/\tilde{d}_{lid}$ (panel a), Equation 15 (panels b–d) or Equation 16 (panel e–f). Insets in temperature plots show details of the temperature profile in the stagnant lid. The dashed black lines are obtained by setting $\tilde{H} = 0$ in Equation 15 (Cartesian cases) or Equation 16 (spherical cases).

$\Delta\eta$ that increases with $\tilde{H}$, and then starts increasing again. For $\tilde{H} < 1$, $\tilde{T}_m$ increases monotonically with $\Delta\eta$, as observed for purely bottom heated convection. Figures S1 and S2, built by solving Equation 21 further illustrate these trends. Note that, for the range of γ expected in ice layers, around 15–20 (Section 5.1), and $\tilde{H} > 1$ one expects $\tilde{T}_m$ to decrease with increasing viscosity ratio.

Table 2
Summary of Scaling Laws

Quantity	Expression	Symbol	Parameters $Ur < 1$	$Ur > 1$
Interior temperature	$\tilde{T}_m = 1 - a_1/f^{a_2}\gamma + (c_1 + c_2 f)\left[\tilde{H}(1 + f + f^2)/3\right]^{c_4}/Ra_{\text{eff}}^{c_3}$	a_1	1.23	1.23
		a_2	1.5	1.5
		c_1	3.5	4.4
		c_2	−2.3	−3.0
		c_3	0.25	1/3
		c_4	1.0	1.72
Surface heat flux	$\tilde{\Phi}_{\text{top}} = aRa_{\text{eff}}^{b}/\gamma^{c}$	a	1.46	1.57
		b	0.27	0.27
		c	1.21	1.21
Stagnant lid thickness	$\tilde{d}_{\text{lid}} = a_{\text{lid}}\gamma^{c}/Ra_{eff}^{b}$	a_{lid}	0.633	0.667
		b	0.27	0.27
		c	1.21	1.21
Threshold internal heating	$\tilde{H}_{\text{crit}} = 3a_H \exp(c_H\gamma)Ra_{\text{surf}}^{b_H}/(1 + f + f^2)$	a_H	0.184	
		b_H	0.31	
		c_H	0.19	

Note. Listed expressions are scaling laws for nondimensional interior temperature, $\tilde{T}_m$, surface heat flux, $\tilde{\Phi}_{\text{top}}$, stagnant lid thickness, $\tilde{d}_{\text{lid}}$, and internal heating at the transition between positive ($Ur < 1$) and negative ($Ur > 1$) bottom heat flux, $\tilde{H}_{\text{crit}}$. In these expressions, $\tilde{H}$ is the internal heating, f the ratio between inner and outer radii (equal to 1 for Cartesian geometry), Ra_{surf} the surface Rayleigh number, and Ra_{eff} the effective Rayleigh number calculated at $\tilde{T} = \tilde{T}_m$ and given by Equation 10. The parameter γ, controlling the amplitude of viscosity changes with temperature, is given by $\gamma = \Delta T/\Delta T_v$, where ΔT_v is the viscous temperature scale (Equation 22). Parameter values are inferred by best fitting these expressions to the results of numerical simulations listed in Table 1.

4.2. Surface Heat Flux

The heat flux through thermal boundary layers (TBL) scales as a power law of the Rayleigh number and of the temperature jump across the TBL (e.g., Moore & Weiss, 1973), implying that in stagnant-lid convection it also scales as the temperature viscous scale. The horizontally averaged nondimensional surface heat flux may then be written as a function of the Rayleigh number and of the parameter γ (Section 4.1), which is, again, equal to ln($\Delta\eta$) in the case of the Frank-Kamenetskii approximation. Figure 4b shows that regardless of $\tilde{H}$, the surface heat flux observed in our simulations with $Ur < 1$ is very well described by the scaling obtained by Deschamps and Lin (2014) and may thus be written

$$\tilde{\Phi}_{\text{top}} = a \frac{Ra_{\text{eff}}^{b}}{\gamma^{c}}, \tag{23}$$

where Ra_{eff} is the effective Rayleigh number (Equation 10), and the constants a, b, and c are equal to 1.46, 0.27, and 1.21, respectively. Spherical cases for $Ur < 1$ also fit well along this parameterization, and do not require any correction for f, as was first suggested by Yao et al. (2014). A reappraisal of Yao et al. (2014) calculations further shows that for $f > 0.6$ such a correction is not needed. Note that $\tilde{\Phi}_{\text{top}}$ implicitly depends on f through Ra_{eff}, which increases with interior temperature $\tilde{T}_m$. Because $\tilde{T}_m$ decreases with f, $\tilde{\Phi}_{\text{top}}$ also decreases with increasing curvature. Interestingly, heat fluxes observed in cases with heterogeneous heating are slightly lower than those predicted by our scaling, but still fit very well along it. This suggests that, at least for $\zeta_{\text{ref}} = 1$ (Equation 9), which implies that dissipation is maximum in the hottest regions, the distribution of heat within the system does not substantially affect the surface heat flux. For $Ur > 1$, our calculations indicate that $\tilde{\Phi}_{\text{top}}$ also fits well along Equation 23 with $a = 1.57$ and values of b and c similar to those for $Ur < 1$ (Figure 4b). Finally, the bottom heat flux, $\tilde{\Phi}_{\text{bot}}$, can easily be calculated by inserting Equation 23 in the nondimensional version of Equation 11.
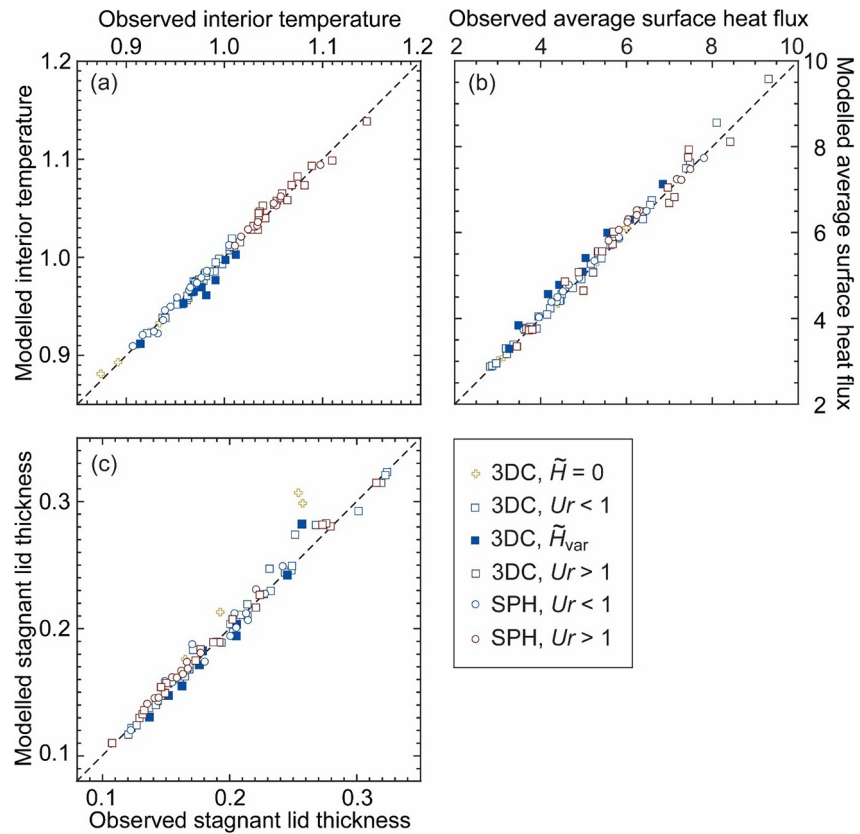
Figure 4. Comparison between observed and modeled output properties. (a) Temperature of the well-mixed interior, $\tilde{T}_m$. Observed values are listed in Table 1, and modeled values are given by Equation 21 with parameter values discussed in Section 4.1. (b) Surface heat flux, $\tilde{\Phi}_{top}$. Observed values are listed in Table 1, and modeled values are calculated by Equation 23 with parameter values discussed in Section 4.2. (c) Thickness of the stagnant lid, $\tilde{d}_{lid}$. Observed values are listed in Table 1, and modeled values are calculated by Equation 26 with parameter values discussed in Section 4.4.

While increasing $\tilde{H}$ results, of course, in larger $\tilde{\Phi}_{top}$ and smaller $\tilde{\Phi}_{bot}$, the influence of the thermal viscosity ratio, $\Delta\eta$, on $\tilde{\Phi}_{top}$ is less intuitive. The $1/\gamma^c$ term and, if γ is not too high, the decrease of $\tilde{T}_m$, both lower $\tilde{\Phi}_{bot}$ as $\Delta\eta$ increases. However, the exponential term in the definition of Ra_{eff} (Equation 10) remains dominant, such that for given values of Ra_{surf} and $\tilde{H}$, $\tilde{\Phi}_{top}$ increases with increasing $\Delta\eta$ (Figure S2). An interesting consequence is that the Urey ratio (Equation 12) decreases with increasing thermal viscosity ratio, as also shown in Table 1. In other words, given the properties (thickness, density, thermal expansion coefficient and diffusivity, temperature jump, gravity acceleration, and rate of internal heating) of a mixed-heated shell animated by stagnant-lid convection, increasing viscosity ratio allows the system to extract more heat from the underlying layer (the bottom heat flux increases). This somewhat counter-intuitive feature results from the strong increase in Ra_{eff} with increasing $\Delta\eta$, implying that convection in the well-mixed interior gets more vigorous.

4.3. Transition Between Positive and Negative Bottom Heat Flux

If internal heating is too large, convection is not efficient enough to evacuate all the produced heat toward the surface. As a consequence, a fraction of this heat is released at the base of the system, resulting in a negative bottom heat flux, $\tilde{\Phi}_{bot}$, and thus, heating up the region located beneath. Setting $\tilde{\Phi}_{bot} = 0$ in Equation 12 provides a criterion for the maximum amount of internal heat that can be transported to the surface as a function of the system properties (Rayleigh number, curvature, and viscosity ratio),

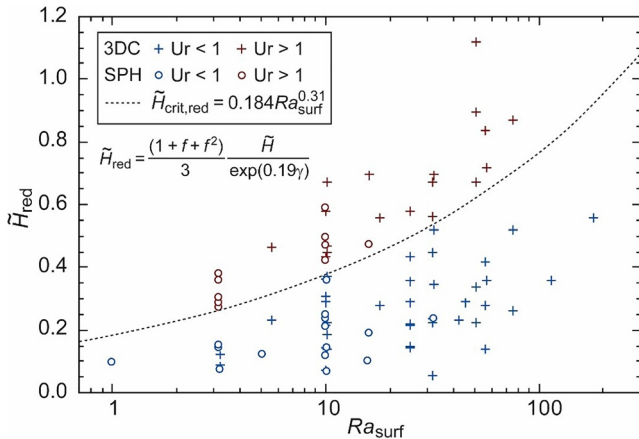$$\tilde{H}_{crit} = \frac{3a}{\left(1 + f + f^2\right)\gamma^c} Ra_{eff}^{\ b}. \tag{24}$$

Figure 5. Reduced nondimensional heating rate, $\tilde{H}_{\text{red}} = \exp(0.19\gamma)(1 + f + f^2)/3$, as a function of surface Rayleigh number, Ra_{surf}. Blue and red symbols plot our numerical simulations (Table 1) with positive and negative bottom heat flux, respectively, and the dashed curve shows the (reduced) critical rate of internal heating for which the bottom heat flux turns negative, $\tilde{H}_{\text{crit}}$, calculated with Equation 25.

Again, because Ra_{eff} depends implicitly (through $\tilde{T}_m$) on $\tilde{H}$, Equation 24 does not have analytical solutions, but can be solved with a zero search method. An additional difficulty in estimating $\tilde{H}_{\text{crit}}$ is that, while the scalings obtained for $Ur < 1$ and $Ur > 1$ overlap at $\tilde{\Phi}_{\text{bot}} = 0$ within the error bars on scaling parameters values, they are not continuous when using the average values of these parameters (Table 2). A simple solution to this problem is to first calculate threshold values of $\tilde{H}$ with both $Ur < 1$ and $Ur > 1$ scalings ($\tilde{H}_{\text{crit}}^-$ and $\tilde{H}_{\text{crit}}^+$, respectively), and second to define the value of $\tilde{H}_{\text{crit}}$ as the average of these two bounds.

We then solved Equation 24 for Ra_{surf} in the range 0.3–300, $\Delta\eta$ in the range 10^4–10^8, and f between 1 (Cartesian geometry) and 0.6, and found that $\tilde{H}_{\text{crit}}$ is well described by

$$\tilde{H}_{\text{crit}} = \frac{3}{\left(1 + f + f^2\right)} a_H \exp\left(c_H \gamma\right) Ra_{\text{surf}}^{b_H} \tag{25}$$

where $a_H = 0.184$, $b_H = 0.31$, and $c_H = 0.19$. Equation 25 provides a convenient way to estimate $\tilde{H}_{\text{crit}}$, and is in good agreement with our simulations (Figure 5). It shows that $\tilde{H}_{\text{crit}}$ increases with Ra_{surf}, $\Delta\eta$, and curvature (decreasing f). Rescaling Equation 25 implies to multiply each of its member by $k\Delta T/\rho D^2$ (Equation 4). Because Ra_{surf} is proportional to D^3, one expects the dimensional critical heating rate, H_{crit}, to decrease approximately as $1/D$. Thus, the transition to a negative heat flux is reached for lower heating rates in thick layers than in thin layers, unless the thermal viscosity ratio and/or the temperature jump increase dramatically with D.

Finally, an interesting result is that, because $\tilde{\Phi}_{\text{bot}}$ increases with the thermal viscosity ratio $\Delta\eta$ (Section 4.2), $\tilde{H}_{\text{crit}}$ also increases with $\Delta\eta$. Therefore, given the properties of a mixed-heated shell animated by stagnant-lid convection, increasing $\Delta\eta$ allows the system to extract heat from the underlying core up to higher rate of internal heating.

4.4. Thickness of the Stagnant Lid

Following Equations 15 and 16, the temperature profile within the lid is not a linear function of depth. However, Figure 3 suggests that these profiles deviate only slightly from a linear function, the discrepancy increasing with the rate of heating. This, in turn, implies that the thickness of this lid should approximately scales as the inverse of the heat flux, leading to

$$\tilde{d}_{\text{lid}} = a_{\text{lid}} \frac{\gamma^c}{Ra_{\text{eff}}^b} \tag{26}$$

where the values of parameters b and c are identical to those for surface heat flux ($b = 0.27$ and $c = 1.21$), and a_{lid} is a constant. Figure 4c shows that Equation 26 provides a good description of the stagnant lid thickness, with best fit to the measured stagnant lid thicknesses obtained for a value of $a_{\text{lid}} = 0.633 \pm 0.03$ for $Ur < 1$, and $a_{\text{lid}} = 0.667 \pm 0.01$ for $Ur > 1$.

5. Application to Europa

We now use the results obtained in Section 4 to estimate the properties of Europa outer ice shell and model its evolution. It is important to note that scaling laws build from quasi-stationary simulations of convection may also be used to describe transient cooling of planetary mantles and ice shells (Choblet & Sotin, 2000; Limare et al., 2021), sustaining the interest of parameterized convection. Our purpose is not to provide a detailed description of Europa's evolution, since we do not consider time-dependent internal heating based on Europa's orbital evolution, but instead to assess quantitatively the role played by tidal heating within the ice layer. This approach can easily be extended to other bodies, including Pluto, which is today tidally locked but may have experienced tidal heating early in its history.

Table 3
Europa and Materials Properties

Parameter	Symbol	Unit	Value/Expression	Europa
Ice Ih properties				
Density	ρ_I	kg/m^3	920	
Thermal expansion coefficient	α_I	1/K	1.56×10^{-4}	
Thermal conductivity	k_I	W/m/K	$566.8/T$	
Heat capacity	C_p	J/kg/K	$7.037T + 185$	
Thermal diffusivity	κ_I	m^2/s	$k/\rho_I C_p$	
Latent heat of fusion	L_I	kJ/kg	284	
Rigidity	μ_I	GPa	4.0	
Reference bulk viscosity	η_{ref}	Pa s	10^{12}–10^{15}	
Activation energy	E	kJ/mol	60	
Liquid water/ammonia properties				
Density (water)	ρ_w	kg/m^3	1,000	
Density (ammonia)	ρ_{NH3}	kg/m^3	734	
Thermal expansion coefficient (water)	α_w	1/K	3.0×10^{-4}	
Heat capacity (water)	C_w	J/kg/K	4,180	
Silicate core properties				
Density	ρ_c	kg/m^3	3,300	
Thermal diffusivity	κ_c	m^2/s	10^{-6}	
Europa properties				
Total radius	R	km		1,561
Core radius	r_c	km		1,400
Gravity acceleration	g	m/s^2		1.31
Surface temperature	T_{surf}	K		100
Reference thermal conductivity	k_{ref}	W/m/K		2.6
Orbital frequency	ω	1/s		2.05×10^{-5}

Note. Liquid ammonia density is taken from Croft et al. (1988), ice rigidity from Roberts and Nimmo (2008), activation energy is taken from the intermediate regime of Durham et al. (2010), and bulk viscosity is a free parameter with possible range of values extended from Montagnat and Duval (2000) estimates. All other data for ice Ih and liquid water properties are similar to that used by Kirk and Stevenson (1987) (see references therein).

A feature common to many (if not all) large icy bodies of the outer solar System is the persistence of a sub-surface ocean beneath an outer ice Ih shell (e.g., Hussmann et al., 2007). In the case of Europa the presence of a sub-surface ocean is supported by anomalies in its external magnetic field, attributed to a magnetic field induced within a sub-surface liquid layer (Khurana et al., 1998). Europa's average density suggests that its rocky core is large, ~70% in volume, corresponding to a radius of ~1,400 km. Given Europa's gravity acceleration, 1.31 m/s^2, the pressure at the surface of the core is not large enough to allow the presence of high pressure ices. Europa's radial structure therefore likely consists of a large rocky core, surrounded by a liquid layer composed of water and impurities, and an outer ice layer. The exact nature of impurities is still debated. Present species may include salts, in particular magnesium sulfate ($MgSO_4$) (Vance et al., 2018), and volatile compounds such as ammonia (NH_3), methanol (CH_3OH), and methane (CH_4), which are all predicted to condensate in giant planets environments with amounts up to a few per cent (e.g., Deschamps, Mousis, et al., 2010; Mousis et al., 2009). The presence of impurities acts as anti-freeze, opposing or delaying the crystallization of the sub-surface ocean. Because it decreases the temperature at the base of the ice shell, it also impacts the dynamics of this shell (e.g., Deschamps & Sotin, 2001). Interestingly, while the exact nature of impurities may affect the sub-surface ocean physical properties, including its density, it does not qualitatively impact the crystallization process, that is, different species present in different amounts would
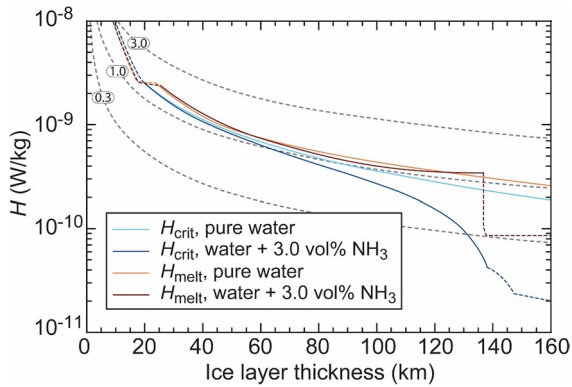
Figure 6. Critical values of internal heating for the transition between a positive and negative bottom heat flux, H_{crit}, and for partial melting of the ice shell, H_{melt}, as a function of the ice shell thickness. Calculations are made with the properties of Europa (Table 3), $\eta_{ref} = 10^{14}$ Pa s, and for two possible compositions of the sub-surface ocean, pure water and an initial mix (i.e., for a shell thickness equal to 0) of water and 3.0 vol% ammonia. Dashed parts of the curves indicate that the system is not animated by convection, based on the observation that the convective heat flux is smaller than the corresponding conductive heat flux. The gray dashed curves represent the heating rate for three values of the total power dissipated within the ice shell (values in TW indicated on each curve).

lead to similar evolutions. For instance, Vilella et al. (2020) pointed out that the impact of 30% $MgSO_4$ on the liquidus is equivalent to that of 3.5% NH_3.

Our modeling approach is detailed in Supporting Information S1. It is mostly similar to the one used in Deschamps (2021a), except for the treatments of the interior temperature, T_m, and of the stagnant lid thickness, d_{lid}. Another important difference is that two sets of parameters are used to calculate T_m and the surface heat flux, Φ_{surf}, depending on whether the bottom heat flux, Φ_{bot}, is positive ($Ur < 1$) or negative ($Ur > 1$) (Table 2). Note that instead of solving Equation 25 to decide which set of parameters to use, we apply a simpler procedure, which accounts for the fact that temperature and heat flux scalings are not continuous at $Ur = 1$. First, we calculate T_m and Φ_{surf} assuming parameter values for $Ur < 1$. If the corresponding Φ_{bot} calculated with Equation 11 is negative, we calculate T_m and Φ_{surf} again, but with parameter values for $Ur > 1$. If the resulting Φ_{bot} turns back to positive, we set arbitrarily its value to zero and recalculate Φ_{surf} and T_m accordingly.

Physical properties of Europa and ice Ih used for calculations are listed in Table 3, and we considered two possible initial compositions for the subsurface ocean, pure water and a mix of water and ammonia. In this later case, we fixed the initial amount of ammonia, x_{NH3}^{init}, to 3.0 vol%, corresponding to about 2.2 wt%. This value may be considered as an upper (possibly exaggerated) bound, and we chose it to obtain a conservative estimate of the impact of impurities on the ice shell properties and evolution. Concentration in ammonia then increases as the ice layer thickens, since only water crystalizes, while impurities are left in the sub-surface ocean. The reference viscosity, η_{ref}, is taken as a free parameter and is varied between 10^{12} and 10^{15} Pa s, a range extended from Montagnat and Duval (2000) estimates of polar ice sheet flow. Results are presented either for a given rate of heating per mass unit, H, or a given total power dissipated in the ice shell, P_{tide}. For an ice shell thickness D_{ice}, H, and P_{tide} are related by (see also Figure S3)

$$H = \frac{3P_{tide}}{4\pi R^3 \left[1 - \left(1 - \frac{D_{ice}}{R} \right)^3 \right]} \tag{27}$$

where R is the total radius of Europa.

5.1. Ice Shell Properties

As heat dissipation in the ice shell increases, two transitions may occur. First, at heating rate H_{crit} the heat flux at the bottom of the shell may turn negative, heating up the underlying sub-surface ocean and delaying its crystallization. Convection can still operate within the ice shell, but would be driven by downwellings and described with scaling laws for $Ur > 1$ (Section 4). Second, at heating rate H_{melt} the bottom temperature exceeds the water liquidus, triggering melting at the bottom of the shell. This implies that the ice shell cannot be thicker than a critical value, D_{melt}. Local pockets of partial melt may further appear in hottest regions (plumes head), introducing additional complexities that are not accounted for by our modeling (see Vilella et al., 2020 for a discussion on this topic). Here, we estimate H_{melt} by comparing the liquidus of pure water with the ice shell horizontally averaged temperature, which underestimates the presence of local pockets of melt. However, because the inverse of the nondimensional viscous temperature scale γ, which is here equal to $E\Delta T/RT_m^2$ (Supporting Information S1), is somewhat high, this bias should be limited (Vilella et al., 2020). Figure 6 shows that both H_{crit} and H_{melt} decrease with increasing ice layer thickness, D_{ice}. The decrease in H_{crit} is mostly related to the thickening of the ice layer (Section 4.3). The decrease in H_{melt} is a consequence of the water liquidus, which is itself decreasing with depth, thus favoring partial melting at lower heating rates. In other words, D_{melt} decreases with increasing H. Taking $H = 10^{-9}$ W/kg and a
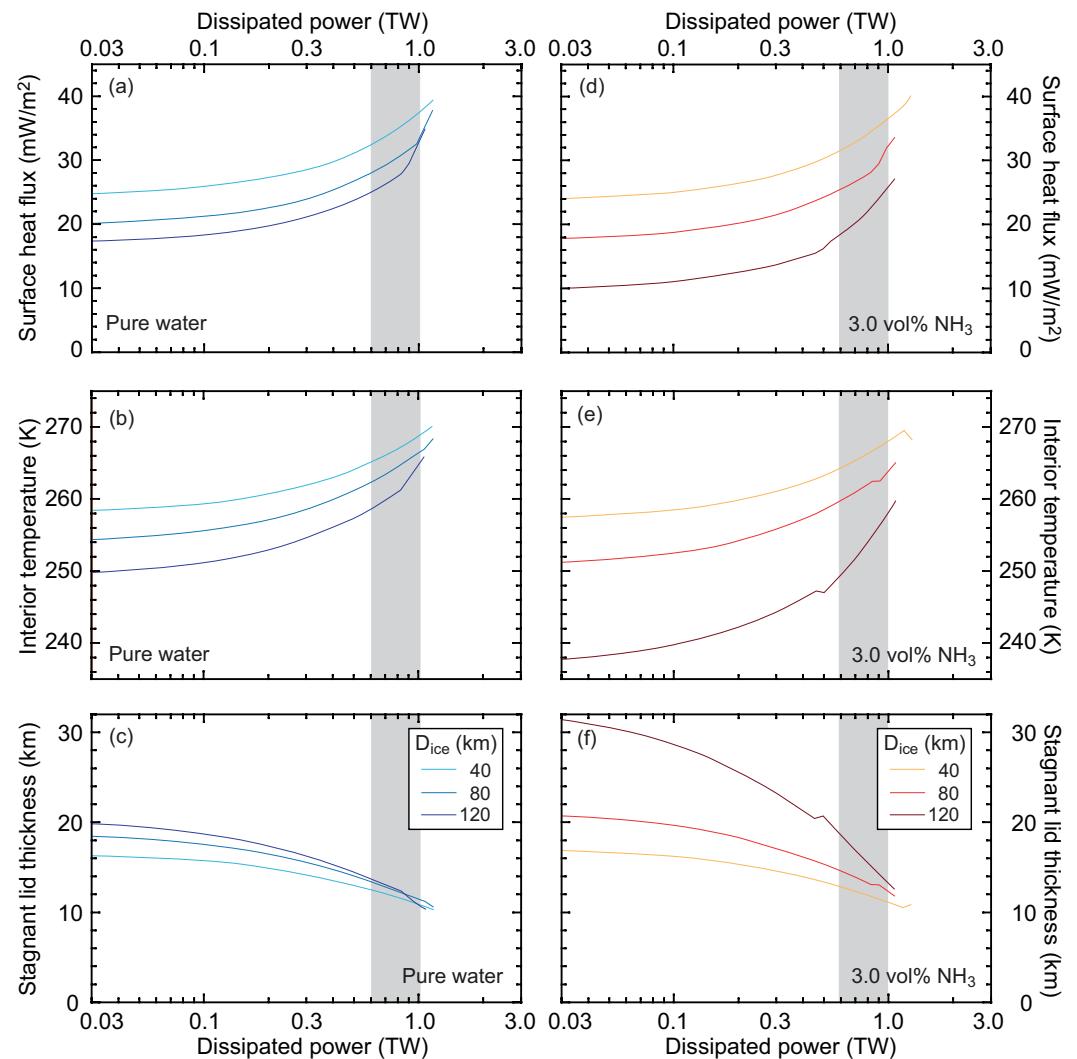
Figure 7. Properties of Europa's outer ice shell as a function of the power dissipated within this shell, and for three selected shell thicknesses (color code). (a and d) Surface heat flux. (b and e) Interior temperature. (c and f) Stagnant lid thickness. Physical properties used for calculations are listed in Table 3, the reference viscosity η_{ref} is equal to 10^{14} Pa s, and two initial compositions of the ocean are considered, pure water (left column), and an initial mix of water and 3.0 vol% ammonia (right column). Curves interruptions indicate that the average interior temperature is larger than the liquidus of pure water at this depth. For the cases with ammonia, two regimes occur depending on whether the Urey ratio (Ur, Equation 12) is smaller or larger than 1, leading to discontinuities at $Ur \sim 1$. The gray shaded bands represent the possible range of dissipated power according to Hussmann and Spohn (2004).

reference viscosity $\eta_{ref} = 10^{14}$ Pa s, for instance, D_{melt} is around 45 km, corresponding to a total power of $\sim$1.2 TW. Figure S4 further indicates that all other parameters being the same, D_{melt} decreases with increasing η_{ref}. As one would expect, in the case of a pure water ocean H_{crit} is very close to H_{melt}. It is also worth noting that the addition of ammonia in the sub-surface ocean moderates the effects of H, allowing slightly thicker ice shells at a given H.

Figure 7 plots the surface heat flux, interior temperature, and stagnant lid thickness as a function of the dissipated power, P_{tide}, and for different shell thicknesses. For the two ocean compositions we tested, and independently of the ice shell thickness, both T_m and Φ_{surf} increase with increasing P_{tide}, while the stagnant lid thins. At a given P_{tide}, thicker shells are cooler and transfer less heat, but these changes attenuate as P_{tide} increases. Interestingly, for values of P_{tide} estimated by Hussmann and Spohn (2004), in the range 0.6–1.0 TW, and despite the fact that the bottom heat flux may turn negative (in particular for cases with NH_3 in the ocean), the ice shell may be as thick as 160 km (see also Figure 6). For slightly larger values, however, D_{melt}
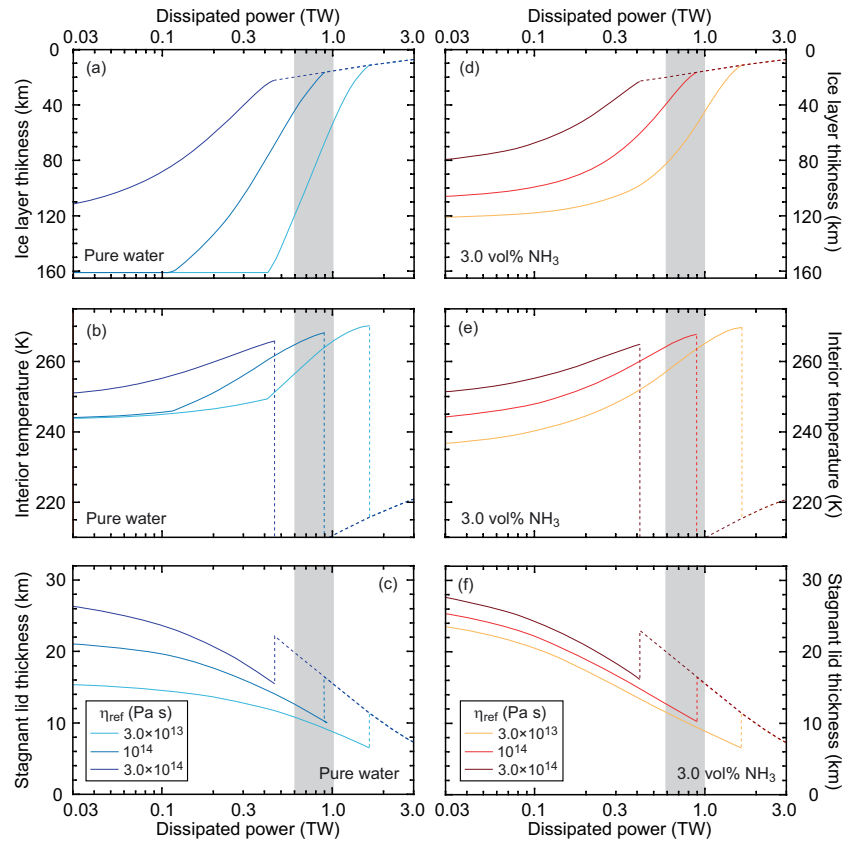
Figure 8. Properties of Europa's outer ice shell at $t = 4.55$ Gyr as a function of the power dissipated within the shell and for three values of the reference viscosity, η_{ref} (color code). (a and d) Thickness. (b and e) Interior temperature. (c and f) Stagnant lid thickness. Physical properties used for calculations are listed in Table 3, and two initial compositions of the ocean are considered, pure water (left column), and an initial mix of water and 3.0 vol% ammonia (right column). Dashed parts of the curves indicate that the system is not animated by convection. The gray shaded bands represent the possible range of dissipated power according to Hussmann and Spohn (2004).

sharply decreases with increasing P_{tide}. In the case of a pure water ocean, for instance, it is equal to 120 and 40 km at P_{tide} of 1.1 and 1.3 TW, respectively. Finally, given D_{ice} and P_{tide}, Φ_{surf} decreases with increasing η_{ref}, while T_m increases and the stagnant lid thickens (Figure S5).

5.2. Thermal Evolution

We model the ice shell thermal evolution following the approach of Grasset and Sotin (1996), solving the conservation equation of energy at the boundary between this shell and the sub-surface ocean (Supporting Information S1). Again, a detailed reconstruction of this evolution would require to couple Europa's internal and orbital evolutions (Hussmann & Spohn, 2004), implying that the tidal power dissipated within the shell is time-dependent. Instead, we assumed that the dissipated heat does not vary with time.

Examples of evolutions for $\eta_{ref} = 10^{14}$ Pa s are shown in Figure S6. The ice shell first thickens up to a maximum value, and then starts to thin again after a time that depends on input parameters. Note that values of P_{tide} around or larger than 1.5 TW prevents the ocean crystallization. The shell remains thinner than 10 km and is not animated by convection. Figures 8 and S7 plot the shell properties at time $t = 4.55$ Gyr as a function of P_{tide} and η_{ref}, respectively. As one could expect, increasing P_{tide} and/or η_{ref} reduces the final shell thickness, D_{ice}, and increases its internal temperature, T_m. In addition, the stagnant lid thickness, d_{lid}, decreases, and convection shuts off at lower η_{ref}. Dissipated powers around or lower than 0.1 TW have no or small impact on D_{ice} and T_m, but still influences d_{lid} substantially. If η_{ref} and/or P_{tide} are too small, the ocean crystallizes completely and remains frozen up to 4.55 Gyr. These conclusions

hold for both a pure water ocean and for an ocean with $x_{\mathrm{NH3}}^{\mathrm{init}} = 3.0$ vol%. In this later case, however, full crystallization cannot be completed even at low η_{ref} and/or P_{tide}. Furthermore, the effects of impurities are reduced as H increases, such that the shell properties get close to those for a pure water ocean. Internal heating therefore appears as a stronger controlling parameter than the presence of impurities. Finally, it is worth noting that for P_{tide} in the range 0.6–1.0 TW, relevant to Europa (Hussmann & Spohn, 2004), and $\eta_{\mathrm{ref}} = 10^{14}$ Pa s, Europa's ice shell should be thin, around 20–40 km at a maximum (see also Figure S6). Lower η_{ref} allows thicker shells, for instance, with $\eta_{\mathrm{ref}} = 3.0 \times 10^{13}$ Pa s, up to 120 km (pure water ocean) or 80 km ($x_{\mathrm{NH3}}^{\mathrm{init}} = 3.0$ vol%).

6. Conclusions and Perspectives

The numerical simulations we performed allowed us to quantify the influence of the rate of internal heating, H, on stagnant-lid convection, through the determination of scaling laws for interior temperature, surface heat flux, and stagnant lid thickness (Table 2). We observed two different regimes depending on the sign of the bottom heat flux, Φ_{bot}, or equivalently, whether the Urey ratio is smaller or larger than 1. Interestingly, our simulations show that the value of H at which Φ_{bot} turns negative increases with increasing thermal viscosity ratio, $\Delta\eta$. Another interesting finding is that, while the stagnant lid stiffens with increasing H, it also thins.

Our simulations of mixed-heated stagnant-lid convection include a few simplifications. First, they were performed for in the Boussinesq approximation. This is an excellent approximation for icy bodies and small rocky planets, but for larger planets, including super-Earths, compressibility should be taken into account. For a strongly temperature-dependent fluid, compressibility substantially modifies the flow pattern, reducing the plume activity and increasing the thickness and strength of stagnant lids (Miyagoshi et al., 2015, 2017). In addition, combining temperature-dependent viscosity and depth-dependent thermal conductivity may lead to the formation of a nearly stagnant layer the bottom of the fluid (Kameyama & Yamamoto, 2018). As a result, our scaling laws should not be used to model systems in which compressibility effects are significant, but they remain a useful tool for studying icy bodies and small planets.

A second limitation of our study is that rheology of ices is certainly more complex than the Frank-Kamenetskii law we used. Compared to an Arrhenius-type of law, this approach overestimates heat flux by up to 30% (e.g., Reese et al., 1999). In addition, different mechanisms may control ice Ih deformation depending on the strain rate and/or the grain size, but are not accounted for in our modeling. A full description of ice viscosity may instead require the definition of a composite viscosity law, as proposed by Harel et al. (2020). Our approach further neglects the possible presence of pockets of partially melted ice. Such pockets may occur in plumes heads, right beneath the stagnant lid, in which case they could trigger the formation of chaos and lenticulae regions (Tobie et al., 2003). Melt may also influence the physical properties of ice, in particular its viscosity and density. This would in turn affect the buoyancy of plumes and reduce tidal dissipation, leading to alternate phases of melting and crystallization (Tobie et al., 2003). Vilella et al. (2020) further studied the impact of melt on heat budget, and showed that for internal heating larger than a critical value, heat flux reaches a plateau, as most of the heating is used to generate more melt. While these limitations may quantitatively alter the scaling laws we build, the main trends indicated by our simulations and the conclusions drawn from them should remain unchanged.

A full description of Europa's ice shell evolution requires coupling its orbital and thermal evolutions to capture time-variations in tidal heating. Interestingly, calculations coupling the evolutions of Io and Europa suggest that tidal dissipation within Europa's ice shell may have remained fairly constant around 0.6–1.0 TW during the past 4.5 Gyr (Hussmann & Spohn, 2004). If true, our evolution model should provide first order, but relevant estimates of today Europa's ice shell properties. For a reference viscosity between 3.0×10^{13} and 3.0×10^{14} Pa s and assuming the presence of impurities, the thickness of this shell should be in the range 20–75 km. This is larger than estimates from mechanical studies based on surface geology observations (e.g., Billings & Kattenhorn, 2005; Damptz & Dombard, 2011; Silber & Johnson, 2017), but consistent with estimates from thermal evolution models (e.g., Allu Peddinti & McNamara, 2019; Green et al., 2021; Hussmann & Spohn, 2004; Tobie et al., 2003) and estimates of the thickness needed to generate melts related to cryovolcanism (Vilella et al., 2020).

In addition to the evolution of icy bodies, our findings may have some implications for the evolution of planetesimals that formed early in solar System history. These bodies are thought to have reached a few hundreds of kilometers in size and to have differentiated in a core and a mantle. The detection of a remanent magnetic field in some meteorites, in particular the pallasite, further suggest that some of these bodies may have developed a magnetic field in their core (e.g., Bryson et al., 2015). The decay of ^{26}Al may have released huge amounts of heat in their mantles, which may, in turn, have delayed the cooling of their cores. The scaling laws we obtained can be inserted in thermal evolution models of planetesimals as built, for instance, by Kaminski et al. (2020). Of particular importance is the fact that, all other parameters being the same, Φ_{bot} increases with increasing $\Delta\eta$ and turns negative for values of H that increase with $\Delta\eta$. This suggests that, if stagnant-lid convection triggered by large top-to-bottom temperature jump, operated within the mantles of planetesimals, the heat flux at the bottom of these mantles may have remained positive even if large amounts of heat were released by the decay of ^{26}Al. The cores of these planetesimals, may have, in turn, started to cool down early after their formation, possibly allowing the generation of magnetic fields within these cores.

Data Availability Statement

The data used for generating the figures displayed in this article are available for academic purposes on Mendeley Data (Deschamps, 2021b). The code used in this work is not publicly available but was thoroughly described in Tackley (2008).

References

Allu Peddinti, D., & McNamara, A. K. (2019). Dynamical investigation of a thickening ice-shell: Implications for the icy moon Europa. *Icarus*, *329*, 251–269. https://doi.org/10.1016/j.icarus.2019.03.037

Billings, S. E., & Kattenhorn, S. A. (2005). The great thickness debate: Ice shell thickness models for Europa and comparisons with estimates based on flexure at ridges. *Icarus*, *177*, 397–412. https://doi.org/10.1016/j.icarus.2005.03.013

Bryson, J. F. J., Nichols, C. I. O., Herrero-Albillos, J., Kronast, F., Kasama, T., Alimadati, H., et al. (2015). Long-lived magnetism from solidification-driven convection the pallasite parent body. *Nature*, *517*, 472–475. https://doi.org/10.1038/nature14114

Choblet, G., & Sotin, C. (2000). 3D thermal convection with variable viscosity: Can transient cooling be described by a quasi-static scaling law? *Physics of the Earth and Planetary Interiors*, *119*, 321–336. https://doi.org/10.1016/s0031-9201(00)00136-9

Christensen, U. R. (1984). Heat transport by variable viscosity convection and implications for the Earth's thermal evolution. *Physics of the Earth and Planetary Interiors*, *35*, 264–282. https://doi.org/10.1016/0031-9201(84)90021-9

Croft, S. K., Lunine, J. I., & Kargel, J. (1988). Equation of state of ammonia-water liquid: .derivation and planetological applications. *Icarus*, *73*, 279–293. https://doi.org/10.1016/0019-1035(88)90098-x

Damptz, A. L., & Dombard, A. J. (2011). Time-dependent flexures of the lithospheres on the icy satellites of Jupiter and Saturn. *Icarus*, *216*, 86–88. https://doi.org/10.1016/j.icarus.2011.07.011

Davaille, A., & Jaupart, C. (1993). Transient high-Rayleigh-number thermal convection with large viscosity variations. *Journal of Fluid Mechanics*, *253*, 141–166. https://doi.org/10.1017/s0022112093001740

Deschamps, F. (2021a). Stagnant lid convection with temperature-dependent thermal conductivity and the thermal evolution of icy worlds. *Geophysical Journal International*, *224*, 1870–1890.

Deschamps, F. (2021b). Scaling laws for mixed-heated stagnant-lid convection and application to Europa. *Mendeley Data*. V1. https://doi.org/10.17632/4hxsj8rw86.1

Deschamps, F., & Lin, J.-R. (2014). Stagnant lid convection in 3D-Cartesian geometry: Scaling laws and applications to icy moons and dwarf planets. *Physics of the Earth and Planetary Interiors*, *229*, 40–54. https://doi.org/10.1016/j.pepi.2014.01.002

Deschamps, F., Mousis, O., Sanchez-Valle, C., & Lunine, J. I. (2010). The role of methanol on the crystallization of Titan's primordial ocean. *The Astrophysical Journal*, *724*, 887–894. https://doi.org/10.1088/0004-637x/724/2/887

Deschamps, F., & Sotin, C. (2000). Inversion of two-dimensional numerical convection experiments for a fluid with a strongly temperature-dependent viscosity. *Geophysical Journal International*, *143*, 204–218. https://doi.org/10.1046/j.1365-246x.2000.00228.x

Deschamps, F., & Sotin, C. (2001). Thermal convection in the outer shell of large icy satellites. *Journal of Geophysical Research*, *106*, 5107–5121. https://doi.org/10.1029/2000je001253

Deschamps, F., Tackley, P. J., & Nakagawa, T. (2010). Temperature and heat flux scalings for isoviscous thermal convection in spherical geometry. *Geophysical Journal International*, *182*, 137–154. https://doi.org/10.1111/j.1365-246x.2010.04637.x

Durham, W. B., Prieto-Ballesteros, O., Goldsby, D. L., & Kargel, J. S. (2010). Rheological and thermal properties of icy minerals. *Space Science Reviews*, *153*, 273–298. https://doi.org/10.1007/s11214-009-9619-1

Grasset, O., & Sotin, C. (1996). The cooling rate of a liquid shell in Titan's interior. *Icarus*, *123*, 101–112. https://doi.org/10.1006/icar.1996.0144

Green, A. P., Montesi, L. G. J., & Cooper, C. M. (2021). The growth of Europa's icy shell: Convection and crystallization. *Journal of Geophysical Research: Planets*, *126*, e2020JE006677. https://doi.org/10.1029/2020JE006677

Guerrero, J., Lowman, J. P., Deschamps, F., & Tackley, P. J. (2018). The influence of curvature on convection in a temperature-dependent viscosity fluid: Implications for the 2D and 3D modeling of moons. *Journal of Geophysical Research: Planets*, *123*, 1863–1880. https://doi.org/10.1029/2017JE005497

Harel, L., Dumoulin, C., Choblet, G., Tobie, G., & Besserer, J. (2020). Scaling of heat transfer in stagnant lid convection for the outer ice shells of icy moons: Influence of rheology. *Icarus*, *338*, 113448. https://doi.org/10.1016/j.icarus.2019.113448

Hussmann, H., Sotin, C., & Lunine, J. I. (2007). Interiors and evolution of icy satellites, in planets and moons. *Treatise on Geophysics*, *10*, 509–539. https://doi.org/10.1016/b978-044452748-6/00168-1

Hussmann, H., & Spohn, T. (2004). Thermal-orbital evolution of Io and Europa. *Icarus*, *171*, 391–410. https://doi.org/10.1016/j.icarus.2004.05.020

Kageyama, A., & Sato, T. (2004). "Yin-Yang grid": An overset grid in spherical geometry. *Geochemistry, Geophysics, Geosystems*, *5*. https://doi.org/10.1029/2004GC000734

Kameyama, M., & Yamamoto, M. (2018). Numerical experiments on thermal convection of highly compressible fluids with variable viscosity and thermal conductivity: Implications for mantle convection of super-Earths. *Physics of the Earth and Planetary Interiors*, *274*, 23–36. https://doi.org/10.1016/j.pepi.2017.11.001

Kaminski, E., Limare, A., Kenda, B., & Chaussidon, M. (2020). Early accretion of planetesimals unravelled by the thermal evolution of the parent bodies of magmatic iron meteorites. *Earth and Planetary Science Letters*, *548*, 116469. https://doi.org/10.1016/j.epsl.2020.116469

Khurana, K. K., Kivelson, M. G., Stevenson, D. J., Schubert, G., Russell, C. T., Walker, R. J., & Polanskey, C. (1998). Induced magnetic field as evidence for subsurface ocean in Europa and Callisto. *Nature*, *395*, 777–780. https://doi.org/10.1038/27394

Kirk, R. L., & Stevenson, D. J. (1987). Thermal evolution of a differentiated Ganymede and implications for surface features. *Icarus*, *69*, 91–134. https://doi.org/10.1016/0019-1035(87)90009-1

Limare, A., Kenda, B., Kaminski, E., Surducan, E., Surducan, V., & Neamtu, C. (2021). Transient convection experiments in internally-heated systems. *MethodsX*, *8*, 101224. https://doi.org/10.1016/j.mex.2021.101224

Miyagoshi, T., Kameyama, M., & Ogawa, M. (2015). Thermal convection and the convective regime diagram in super-Earths. *Journal of Geophysical Research: Planets*, *120*, 1267–1278. https://doi.org/10.1002/2015je004793

Miyagoshi, T., Kameyama, M., & Ogawa, M. (2017). Extremely long transition phase of thermal convection in the mantle of massive super-earths. *Earth Planets and Space*, *69*, 46. https://doi.org/10.1186/s40623-017-0630-6

Montagnat, M., & Duval, P. (2000). Rate controlling processes in the creep of polar ice, influence of grain boundary migration associated with recrystallization. *Earth and Planetary Science Letters*, *183*, 179–186. https://doi.org/10.1016/s0012-821x(00)00262-4

Moore, D. S., & Weiss, N. O. (1973). Two-dimensional Rayleigh-Bénard convection. *Journal of Fluid Mechanics*, *58*, 289–312. https://doi.org/10.1017/s0022112073002600

Moore, W. B. (2008). Heat transport in a convecting layer heated from within and below. *Journal of Geophysical Research*, *113*. https://doi.org/10.1029/2006JB004778

Moresi, L.-N., & Solomatov, V. S. (1995). Numerical investigation of 2D convection with extremely large viscosity variations. *Physics of Fluids*, *7*, 2154–2162. https://doi.org/10.1063/1.868465

Mousis, O., Lunine, J. I., Thomas, C., Pasek, M., Marboeuf, U., Alibert, Y., et al. (2009). Clathration of volatiles in the Solar nebula and implications for the origin of Titan's atmosphere. *The Astrophysical Journal*, *691*, 1780–1786. https://doi.org/10.1088/0004-637x/691/2/1780

Parmentier, E. M., & Sotin, C. (2000). Three-dimensional numerical experiments on thermal convection in a very viscous fluid: Implications for the dynamics of a thermal boundary layer at high Rayleigh number. *Physics of Fluids*, *12*, 609–617. https://doi.org/10.1063/1.870267

Reese, C. C., Solomatov, V. S., Baumgardner, J. R., & Yang, W.-S. (1999). Stagnant-lid convection in a spherical shell. *Physics of the Earth and Planetary Interiors*, *116*, 1–7. https://doi.org/10.1016/s0031-9201(99)00115-6

Roberts, J. H., & Nimmo, F. (2008). Tidal heating and the long-term stability of a subsurface ocean on Enceladus. *Icarus*, *194*, 675–689. https://doi.org/10.1016/j.icarus.2007.11.010

Silber, E. A., & Johnson, B. C. (2017). Impact crater morphology and the structure of Europa's ice shell. *Journal of Geophysical Research: Planets*, *122*, 2685–2701. https://doi.org/10.1002/2017je005456

Solomatov, V. S. (1995). Scaling of temperature- and stress-dependent viscosity convection. *Physics of Fluids*, *7*, 266–274. https://doi.org/10.1063/1.868624

Solomatov, V. S., & Moresi, L.-N. (1997). Three regimes of mantle convection with non-Newtonian viscosity and stagnant lid convection on the terrestrial planets. *Geophysical Research Letters*, *24*, 1907–1910. https://doi.org/10.1029/97gl01682

Sotin, C., & Labrosse, S. (1999). Three-dimensional thermal convection in an iso-viscous, infinite Prandtl number fluid heated from within and from below: Applications to the transfer of heat through planetary mantles. *Physics of the Earth and Planetary Interiors*, *112*, 171–190. https://doi.org/10.1016/s0031-9201(99)00004-7

Stein, C., Lowman, J. P., & Hansen, U. (2013). The influence of mantle internal heating on lithospheric mobility: Implications for super-Earths. *Earth and Planetary Science Letters*, *361*, 448–459. https://doi.org/10.1016/j.epsl.2012.11.011

Tackley, P. J. (2008). Modelling compressible mantle convection with large viscosity contrasts in a three-dimensional spherical shell using the yin-yang grid. *Physics of the Earth and Planetary Interiors*, *171*, 7–18. https://doi.org/10.1016/j.pepi.2008.08.005

Tarantola, A., & Valette, B. (1982). Generalized nonlinear inverse problems solved using the least square criterion. *Reviews of Geophysics and Space Physics*, *20*, 219–232. https://doi.org/10.1029/rg020i002p00219

Tobie, G., Choblet, G., & Sotin, C. (2003). Tidally heated convection: Constraints on Europa's ice shell thickness. *Journal of Geophysical Research*, *108*. https://doi.org/10.1029/2003JE002099

Tobie, G., Mocquet, A., & Sotin, C. (2005). Tidal dissipation within large icy satellites: Applications to Europa and Titan. *Icarus*, *177*, 534–549. https://doi.org/10.1016/j.icarus.2005.04.006

Travis, B., & Olson, P. (1994). Convection with internal sources and turbulence in the Earth's mantle. *Geophysical Journal International*, *118*, 1–19. https://doi.org/10.1111/j.1365-246x.1994.tb04671.x

Vance, S. D., Panning, M. P., Stähler, S., Cammarano, F., Bills, B. G., Tobie, G., et al. (2018). Geophysical investigations of habitability in ice-covered ocean worlds. *Journal of Geophysical Research: Planets*, *123*, 180–205. https://doi.org/10.1002/2017je005341

Vilella, K., Choblet, G., Tsao, W. E., & Deschamps, F. (2020). Tidally heated convection and the occurrence of melting in icy satellites: Application to Europa. *Journal of Geophysical Research: Planets*, *125*, e2019JE006248. https://doi.org/10.1029/2019JE006248

Vilella, K., & Deschamps, F. (2018). Temperature and heat flux scaling laws for isoviscous infinite Prandtl number mixed heating convection. *Geophysical Journal International*, *214*, 265–281. https://doi.org/10.1093/gji/ggy138

Yao, C., Deschamps, F., Lowman, J. P., Sanchez-Valle, C., & Tackley, P. J. (2014). Stagnant-lid convection in bottom-heated thin 3-D spherical shells: Influence of curvature and implications for dwarf planets and icy moons. *Journal of Geophysical Research: Planets*, *119*, 1895–1913. https://doi.org/10.1002/2014je004653